International Journal of Plasticity 128 (2020) 102660

Contents lists available at ScienceDirect

International Journal of Plasticity

journal homepage: http://www.elsevier.com/locate/ijplas

Strain hardening, twinning and texture evolution in magnesium alloy using the all twin variant polycrystal modelling approach

Sudeep K. Sahoo [a], Somjeet Biswas [a,*], Laszlo S. Toth [b,c], P.C. Gautam [a], Benoît Beausir [b,c]

[a] *Department of Metallurgical and Materials Engineering, Indian Institute of Technology, Kharagpur, West Bengal, 721302, India*
[b] *Laboratoire D'Etude des Microstructures et de Mécanique des Matériaux (LEM3), CNRS UMR 7239, Université de Lorraine, 57045, Metz Cedex 1, France*
[c] *Laboratory of Excellence on Design of Alloy Metals for Low-mAss Structures (DAMAS), Université de Lorraine, Metz, France*

ARTICLE INFO

Keywords:
Magnesium
Texture
Polycrystal modelling
Extension twins
Strain hardening
All twin variants approach

ABSTRACT

In this work, the viscoplastic self-consistent based All Twin Variant (ATV) polycrystal modelling was employed to decipher the deformation behaviour of Mg–3Al-0.3Mn Magnesium alloy that develops $\{10\overline{1}2\}\overline{1}011$ - extension twins profoundly during ambient temperature compression. Twinning was considered by taking into account all the potential $\{10\overline{1}2\}$ – twin variants, and hence called here as the 'ATV' approach. The model treats each twin variant as a grain with increasing volume fraction transferred from the respective parent grain according to its pseudo-slip shear-rate. The slip and twin-induced strain hardening were simulated by adopting a classical phenomenological hardening model while assigning a higher hardening coefficient for the twins relative to the parent matrix. The viscoplastic self-consistent polycrystal homogenisation scheme combined with the ATV approach permitted to reproduce with high precision the experimentally measured strain hardening behaviour, crystallographic texture and twin volume fraction evolution. Beyond these average measures, the activities of twin variants in individual grains could be predicted in good agreement with Electron Back-Scattered Diffraction measurements. The ATV approach permits also to examine the matrix and twin phases separately in terms of textures and misorientation distributions.

1. Introduction

Deformation-induced twinning plays a dominant role in tailoring the microstructure in hexagonal close packed (HCP) Magnesium (Mg) alloys. Inevitably, such twin induced plastic deformation becomes quite apparent at low homologous temperatures, where the contribution of slip-induced deformation is limited (Barrett and Haller, 1947; Kelley and Hosford, 1968; Christian and Mahajan, 1995; Barnett, 2007; Graff et al., 2007; Jiang et al., 2008; Dudamell et al., 2011; Khan et al., 2011). Although several types of twins have been reported so far (Yoo, 1981; McCabe et al., 2009; Bozzolo et al., 2010; Knezevic et al., 2015), the most commonly recognized deformation twins in Mg alloys are $\{10\overline{1}2\}\overline{1}011$ - extension twins (Pei et al., 2012; Ma et al., 2012; El Kadiri et al., 2013b, 2015; Dixit et al., 2015). Deformation-induced extension twin results in lattice reorientation by ~86.4° about the $11\overline{2}0$ axes with respect to the parent orientation (Yoo, 1981; Christian and Mahajan, 1995; Knezevic et al., 2010; Niewczas, 2010; Ardeljan et al., 2016). As a consequence,

* Corresponding author.
E-mail address: somjeetbiswas@metal.iitkgp.ac.in (S. Biswas).

https://doi.org/10.1016/j.ijplas.2020.102660
Received 20 June 2019; Received in revised form 1 January 2020; Accepted 3 January 2020
Available online 15 January 2020

its influence can be readily marked by two key aspects: (i) rapid texture evolution with strain, which depends on the activated twin variants, and (ii) increase in strain hardening rate (Yoo, 1981; Barnett et al., 2004; Lou et al., 2007; Fernández et al., 2011; Khan et al., 2011; Wang et al., 2012; Ando et al., 2014; Mu et al., 2014; Kabirian et al., 2015). The twin-induced hardening response could be well deciphered in terms of: (i) geometrical hardening due to abrupt crystallographic reorientation from softer-parent domain to harder-twin orientations (Agnew et al., 2003; Jain and Agnew, 2007; Jiang et al., 2007b; Lou et al., 2007; Knezevic et al., 2010; Dixit et al., 2015), (ii) Hall-Petch type hardening due to grain subdivision (Salem et al., 2003; Proust et al., 2009), and (iii) Basinski type hardening (Basinski et al., 1997), due to transmutations of dislocations from glissile to sessile at the twin interfaces (Knezevic et al., 2010, 2015; Zhang and Joshi, 2012; Jahedi et al., 2017; Zilahi, 2018; Allen et al., 2018). There are theoretical and experimental works which show that the dislocation density is higher in the twins than in the matrix grains (Oppedal et al., 2012; Allen et al., 2018; Zilahi, 2018). The mechanisms underlying the plastic deformation can be well understood by linking simulation/modelling studies with the experimental results. To account for this, several simulation studies exist ranging from (i) micro-scale, i.e., molecular and dislocation dynamics at the atomic level; (ii) mesoscale, i. e, viscoplastic self-consistent models (VPSC), crystal plasticity finite element models at the grain level, and (iii) continuum scale finite element methods at the structural level, as well as multi-length scale approaches (Raabe, 1998; Roters et al., 2010; Friák et al., 2011; Eisenlohr et al., 2013; Gurao and Suwas, 2014; Paramatmuni and Kanjarla, 2018).

Till date, a variety of crystal plasticity approaches have been proposed and proved to be an efficient tool in deciphering the twin-induced mechanical behaviour. To tailor such behaviour, mean-field models such as Taylor (1938) or self-consistent (Molinari et al., 1987) schemes are used as a platform. The first computational approach incorporating deformation twinning was proposed by Van Houtte (1978), where a Monte Carlo scheme was used to replace a grain completely with a twin, considering twinning as a pseudo-slip mechanism. Further, Tomé et al. (1991) put forward two more approaches to account for crystallographic reorientation due to deformation twins within the grains. The first is the predominant twin reorientation (PTR) scheme, which is based upon identifying the active twin variant with the highest accumulated volume (predominant twin). In their approach, when the twinning activity in a given grain attains a critical value, the entire grain is completely replaced by its corresponding predominant twin orientation. Tomé et al. (1991) established a volume fraction transfer (VFT) scheme where the contribution towards texture evolution is taken into account through the transfer of volume fraction from one "voxel" to another in the Euler space for each twinning variant. This approach permitted to obtain the twin-affected texture evolution using a constant number of grains where each voxel represents a single grain. However, the drawback of both of these approaches is that the identity of the parent grain is lost. Nevertheless, successful simulations for both texture and twin volume evolution were possible by both the PTR and VFT schemes (Tomé et al., 1991, 2001; Karaman et al., 2000).

Alternatively, within the framework of large strain crystal plasticity, Kalidindi (1998) proposed to create all twin variants as grains for each "parent orientation" before the commencement of deformation. In that approach, the growth of the twins was modelled via the gradual transfer of volume from the parent grain to the twins according to their shear-rates using the Taylor model in large strain formalism. We call this twinning approach as the All Twin Variant ('ATV') approach. This modelling is an improvement of the VFT approach previously introduced by Tomé et al. (1991). Later, Kalidindi (2001) and his co-workers (Salem et al., 2003) introduced a hardening scheme that considers the evolution of activation stress for the slip and twinning systems with deformation. The interactions between slip and twinning were modelled by employing a latent hardening coefficient as a function of the coplanarity between slip and twin planes. On the other hand, Tomé et al. (2001) also implemented a latent hardening approach within the viscoplastic self-consistent code while employing the PTR approach to compute the mechanical response and texture evolution simultaneously for Zirconium under simple compression and tension.

A more sophisticated approach was presented by Tomé and Kaschner (2005) and later by Proust et al. (2007) adopting the lamellar grain model of Lebensohn (1999) to account for the twin shape, and twin-parent interaction referred to as the composite grain (CG) model. The growth of twin was modelled by partitioning the grain into parallel representative twin inclusions embedded into the parent grain. The predominating twin system was chosen as the active variant. The model was initially applied to address the role of twinning during strain path changes in Zr (Tomé and Kaschner, 2005) and later was extended to involve the effect of de-twinning in Mg due to strain path change (Proust et al., 2007). The hardening effect was taken into account via the Voce type hardening law while considering the directionality of grain refinement via the Hall-Petch relationship.

Several phenomenological constitutive approaches were introduced for enriching the physical aspects of the twinning behaviour, e. g. nucleation, propagation and growth. In this regard, a model introducing the nucleation phenomena of deformation twins was proposed by Robson et al. (2010), Beyerlein and Tomé (2010) and Beyerlein et al. (2011). An experimental statistical analysis was carried out by Beyerlein et al. (2010) for twinning activity in pure Mg under compression. They evidenced the effect of neighbouring grains on the nucleation and growth of twin variants commencing at the grain boundaries. Their main observation was that twin nucleation and growth depends not only on the orientation of the grain but also on the neighbours, especially on the misorientation of the grain boundary. Further, Mu et al. (2011, 2014) introduced different critical resolved shear stresses (CRSS) for twin nucleation and growth to consider the effect of stress relaxation in the twin by imposing higher CRSS for nucleation with respect to twin growth. The approach used a cluster type grain interaction Taylor model ('GIA') to account for twinning during the texture evolution of AZ31 while adopting the PTR scheme of Tomé et al. (1991). The effect of hardening was modelled based on the total dislocation density evolution and the mean free path for dislocation glide via a Kocks-Mecking type parameter. Homayonifar and Mosler (2011, 2012) proposed a crystal plasticity model by incorporating deformation twinning based on energy minimization. El Kadiri and Oppedal (2010) and El Kadiri et al. (2013a) utilised crystal plasticity to investigate the mechanical characteristics induced by deformation twinning in HCP metals. Recently, Tadano et al. (2016) presented a crystal plasticity model to explicitly capture the evolution of twin volume fraction by deriving a constitutive equation superimposing the untwinned and twinned regions.

It is worth noting that all these models mentioned in the previous paragraph employ the PTR scheme to capture the twin-induced texture evolution; except for the ATV and VFT approaches. It can be debated that less active twin variants may also play an important role in texture evolution. Nave and Barnett (2004), El Kadiri et al. (2013a), Mu et al. (2014), and Mokdad et al. (2017) experimentally demonstrated that during plastic deformation, lenticular shape twins develop with parallel or crossing type morphology depending on the crystallographic orientation and the local stress state. They speculated that the presence of such morphological feature is the consequence of twins belonging to different variants. With progressive deformation, these extension twins expand in volume within the grain and sometimes engulfs a significant portion of the entire grain. Though all extension twin variants may not be activated simultaneously during plastic deformation (Park et al., 2010; Martin et al., 2010; Xin et al., 2016; Mokdad et al., 2017; Hazeli et al., 2018), the activity of specific variants potentially contributes towards the development of a particular texture component. Therefore, it is imperative to focus on all twin variants' activity that may evolve during a real deformation and to develop a comprehensive model to simulate the twin induced deformation behaviour. Under this premise, Gu and Toth (2012, 2014) adopted the ATV scheme approach initially proposed by Kalidindi (1998) to represent twinning and de-twinning activities in the microstructure during low-cycle deformation of AZ31 at room temperature within the framework of the Taylor–Lin polycrystal model. In their work, they identified the number of operating twin variants on a grain-by-grain basis, in agreement with the experimental measurements, for 95% cases. Further, the ATV model was also used to predict the texture evolution during ECAP of Mg alloy (Gu et al., 2013). Toth et al. (2018) used the ATV model for TWIP steel in ECAP, for strain hardening and texture evolution; they included even secondary twinning. Dancette et al. (2012) also used all twinning variants in a crystal plasticity finite element approach for predicting strain hardening, texture evolution and local twinning activities for a TWIP steel. Hence, it is reasonable to state that the ATV approach had been used so far in the works of Gu and Toth (2012, 2013, 2014), Toth et al. (2018), and Dancette et al. (2012). The basic principle of ATV modelling is that no specific variant selection technique is implemented to favour certain twin variants; all of them are subjected to the same modelling conditions.

Sahoo et al. (2019) introduced an analytical approach that could capture strain hardening and twin volume evolution during profound extension twinning in Mg–3Al-0.3Mn. The study indicated that the observed strain hardening is the combined effect of geometrical (textural) hardening due to the reorientation of the matrix into twins and intrinsic dislocation hardening. The analysis revealed that the Hall-Petch hardening is minimal, as the $\{10\bar{1}2\}$- Extension twins do not produce significant grain refinement. This finding is consistent with previous observations (Knezevic et al., 2010; Dudamell et al., 2011; Oppedal et al., 2012; Dixit et al., 2015; Molodov et al., 2017) and demonstrated that extension twins develop at very low strains (˂0.035), then quickly grow to encompass the entire parent grains without imposing an appreciable barrier effect to slip. This is due to the transmission of dislocations readily through the extension twin boundaries in Mg. Moreover, a larger strain is required for the increased dislocation density necessary for Basinski-type hardening effect. Though twins develop at the early stage when the dislocation density is not significantly high, the continued slip of dislocations into the twins results in irreversible transmutation of dislocations into the twins at higher strains, so the twins harden faster than the matrix (Oppedal et al., 2012; Wang and Agnew, 2016; Zhang et al., 2017; Allen et al., 2018).

1.1. *Scope of the article*

In this work, we are presenting a polycrystal simulation work using the VPSC model of Molinari et al. (1987) in its finite element-tuned version (Molinari and Toth (1994)) to account for twin-induced deformation behaviour of Mg–3Al-0.3Mn under compression. Twinning was handled using the ATV approach, where for every initial 'parent grain', all its corresponding extension twin variants were created as new grains and added to the initial polycrystal with zero starting volume fraction. Thereafter during plastic deformation, a fraction of the parent grain was allocated to the respective twin-grains based upon their pseudo-slip shear rate. Self and latent hardening were employed with different hardening coefficients for both the parent and the twin matrix while considering twins to be harder as compared to that of the parent matrix. The ATV approach could reproduce the average properties, such as crystallographic texture, strain hardening and twin activity in good agreements with the experimental counterparts. There was no specific variant selection criterion adopted for twinning, rather the activity of the twin variants was computed from their respective shear rate. Nucleation was not modelled as all variants were considered, independently of the neighbouring grains. It has been shown that the ATV approach can be used to examine the simulated extension twin variants and their respective volume fraction by comparing them with experiments on individual grain basis. For this purpose, 45 parent grains with different orientation were randomly selected from the electron back-scattered diffraction (EBSD) maps. Four cases were analysed and presented in detail. The overall good agreements between simulation and experiment for the texture, strain hardening and twinning activities in individual grains fully validate the ATV approach.

2. Polycrystal modelling framework

2.1. *Principles of the "All twinning variants" (ATV) Approach*

In HCP Mg alloys, six $\{10\bar{1}2\}$-extension twin variants exist and may evolve during deformation. They develop with a lamellar/ lenticular morphology while appearing to be intersecting with each other or parallel to one another within the parent grains during deformation (Nave and Barnett, 2004; El Kadiri et al., 2013a; Mu et al., 2014; Mokdad et al., 2017). Geometrically, these six $\{10\bar{1}2\}$extension twin variants are reoriented at 86.4° about the six $\langle 11\bar{2}0\rangle$ axes from the parent grain, as shown in Table 1. In the ATV approach, all these variants are created before the simulation and incorporated into the polycrystal population with initially zero volume fractions. The principles of the ATV approach were introduced by Kalidindi (1998) for predicting the texture evolution while using the Taylor model. In the present work, we use the VPSC polycrystal model in an incremental form with large strain formalism, following the Eulerian approach. Additionally, the VPSC model permits to take into account the effect of grain shape. This is especially important for twins as they appear to adopt a lamellar shape. The initial parent grains were assumed to be spherical, and with increasing strain, they were allowed to change their shape gradually into ellipsoids. On the contrary, the twin variants were characterized by oblate ellipsoids with thickness 't' and diameter 'l' which define the aspect ratio by $q = t/l$. The shortest axis of the ellipsoid was parallel to the normal of the twinning plane K_1, whereas the other two axes were taken equal and lying in the twinning plane (see Fig. 1). The initial aspect ratio 'q' was taken 0.2, and the shapes of the twin were allowed to evolve with strain according to their displacement gradient field obtained within the VPSC framework. Nevertheless, as the compression strain was relatively small, the already very flat twin-grains did not change their aspect ratio significantly.

The growth of the twin variants were modelled by assigning them a part of the volume from their respective parent grains in each incremental strain. This was determined by the amount of shear for a given twin system within the parent grain during deformation with respect to the maximum shear value for 100% twinning (γ_{twin}). Henceforth, the volume allocation from the parent grain to the twin variants (ΔV_s) during a time increment Δt was incremented numerically according to the following formula:

$$\Delta V_s = V_{parent} \times \frac{\left|\dot{\gamma}^{s}_{twin}\right| \Delta t}{\gamma_{twin}}. \tag{1}$$

Here V_{parent} is the actual volume of the parent grain and γ_{twin} is the characteristic shear strain for extension twinning in Mg (0.131). The ratio $\left|\dot{\gamma}^{s}_{twin}\right|/\gamma_{twin}$ is the fraction of the shear rate of the twin system with respect to the twin-shear. Once a twin had non-zero volume fraction, it was considered to be a grain and crystallographic slip was allowed to take place within it. Since secondary twinning was not observed in the experiments, the twinning systems were not considered within the twins for their further plastic deformation. That is, secondary twinning was not modelled. (Note that modelling secondary twinning would have required a much more complex program and an increase in the number of grains by a factor of six.)

2.2. Hardening law

Twinning has a significant role in influencing the strain hardening response. This is due to its inherent harder nature compared to the parent matrix (Agnew et al., 2003; Knezevic et al., 2010; Dixit et al., 2015; Sahoo et al., 2019). In this aspect, strain hardening was modelled using the self and latent hardening approach proposed by Kalidindi et al. (1992) and Zhou et al. (1993). In that approach, the slip resistance of a slip system $\tau_0^{(i)}$ is governed by the following relation:

$$\dot{\tau}_0^{(i)} = \sum_{j=1}^{N} H^{ij} \left|\dot{\gamma}^{j}\right| \text{ where i, j } = 1, \&\&., \text{ N}. \tag{2}$$

Here, i and j are the indices of the slip systems, $\dot{\gamma}^{j}$ is the slip rate, N is the total number of slip and twinning systems, and the H^{ij} quantity is the hardening matrix (dimension: N x N). It is defined by:

$$H^{ij} = q^{ij} h_0 \left(1 - \frac{\tau_0^{i}}{\tau_{sat}}\right)^{a}. \tag{3}$$

Here, h_0 and a are hardening parameters, τ_{sat} is the saturation stress. The matrix q^{ij} describes the self and latent interactions between slip systems. The elements of this hardening matrix were determined according to four possible geometrical configurations of the i and j slip systems by imposing constants values for coplanar slip (q_1), collinear slip (q_2), perpendicular slip (q_3) between two slip systems i and j. For all other configurations, the coefficient (q_4) was allocated. Note that this hardening matrix is very different from the one proposed by Parisot et al. (2004) where the q^{ij} values are grouped according to slip system families (with prismatic slip parameter not being constant). The above equations (2) and (3) hold separately for both the parent and twins. A higher hardening coefficient (h_0) for

Table 1
Nomenclature for the extension twin variants on the basis of K_1 plane and η_1 direction and its corresponding rotation axis about which the twin orientations are rotated by ~86.4° with respect to the parent grain. T_{ij} represents the twin variants, where i = 1, 2, 3 designates the different twin variants and j = a, b represents the variants belonging to the same pair.

Twin Variants (T_{ij})	Twinning plane and direction	Rotation axis about parent grain
T_{1a}	$(\bar{1}102)\ [1\bar{1}01]$	$[11\bar{2}0]$
T_{2a}	$(\bar{1}012)\ [10\bar{1}1]$	$[\bar{1}2\bar{1}0]$
T_{3a}	$(0\bar{1}12)\ [01\bar{1}1]$	$[2\bar{1}\bar{1}0]$
T_{3b}	$(01\bar{1}2)\ [0\bar{1}11]$	$[\bar{2}110]$
T_{2b}	$(10\bar{1}2)\ [\bar{1}011]$	$[1\bar{2}10]$
T_{1b}	$(1\bar{1}02)\ [\bar{1}101]$	$[\bar{1}\bar{1}20]$

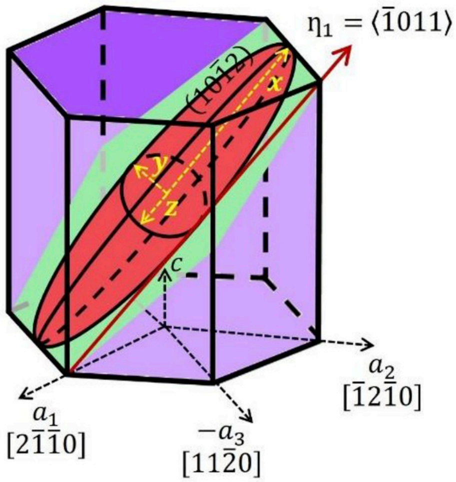

Fig. 1. Schematic representation of the extension twin ($K_1 = (10\bar{1}2)$, $\eta_1 = \langle\bar{1}011\rangle$) with ellipsoidal shape used in the model within the HCP unit cell.

the twins was assigned with respect to the parent matrix, such that a higher hardening rate for the twins could be achieved. It is to be noted that this crystal plasticity hardening approach was simplified in a recent work by Sahoo et al. (2019) to be useable in a phenomenological strain hardening model for twinning in Mg.

2.3. Basic elements of the VPSC model

The present crystal plasticity simulation work is based on the VPSC model established by Molinari et al. (1987). This VPSC approach was slightly improved using finite element tuning by Molinari and Toth (1994) where a scalar coefficient (α) was introduced into the interaction equation between a grain and the whole polycrystal:

$$s^g - S = \alpha\left(\Gamma^{sgg-1} + A^s\right)(d^g - D). \tag{4}$$

Here, s^g and d^g represent the deviatoric stress state and the strain-rate state in grain g, respectively. S and D are the macroscopic deviatoric stress and strain rate. A^s stands for the macroscopic secant modulus, and Γ^{sgg} is the interaction tensor which accounts for the shape effects of the grains. The strength of the interaction between the grain and the homogeneous equivalent medium constituted by the whole polycrystal is governed by the parameter α. By modifying the value of α, different modelling conditions can be achieved, i.e. static (α = 0), tangent (α = m), secant (α = 1) and Taylor (α = ∞). Thus, by increasing the α value, the major effect is to decrease the differences between the local and macroscopic strain rate states, i.e., less heterogeneity. In Molinari et al. (2004) it was shown that for both spherical and elliptical shapes $\alpha = m$, where m is the strain rate sensitivity exponent for the slip. This is actually the so-called tangent approach, initially introduced by Molinari et al. (1987). In the VPSC model, the stress and strain in each grain can be different from the macroscopic values. The self-consistency condition is that the averages of the strain rates and the deviator stresses in the grains have to satisfy the following:

$$\langle d^g\rangle = D; \quad \langle s^g\rangle = S. \tag{5}$$

where ⟨ . ⟩ means the arithmetic volume average over the polycrystalline aggregate.

Plasticity in each grain is considered by the activation of slip and twin systems. For both crystallographic slip and twinning, the shear rates ($\dot{\gamma}^s$) in both the slip and twinning systems are linked to the resolved shear stress (τ^s) via the strain rate dependent constitutive law developed by Hutchinson (1976):

$$\dot{\gamma}^s = \dot{\gamma}_0 \;\; sign\left(\tau^s \big/ \tau_0^s\right)\left|\left|\tau^s \big/ \tau_0^s\right|\right|^{1/m} \tag{6}$$

Here, τ_0^s is the reference resolved shear stress corresponding to the reference slip rate $\dot{\gamma}_0$. The slip systems are grouped into slip system 'families' and their activity may differ from one family to others. The τ_0^s quantities are initially the same within one family but vary with strain according to the hardening law presented above, so that they can become different from one slip system to another within the same family. The $\dot{\gamma}_0$ parameter can be taken the same for all slip and twinning systems.

Likewise, the same constitutive law (Eq. (6)) was employed for the twinning systems, by considering them as pseudo-slips. Twinning activity is unidirectional, which means that twinning can happen only in one crystallographic direction on the twinning plane; the opposite is excluded. As a consequence, among all twin systems, only a few of them get activated. On the contrary, for slip, both slip directions are possible on the same slip plane.

It is to be noted that in a VPSC modelling approach the stress and strain rate states are considered homogeneous within a grain (albeit different from the macroscopic one), hence does not permit to consider the effects of heterogeneous stress and strain on the nucleation or growth of a twin variant. Nevertheless, it is important to see to what extent the VPSC model can predict the experimental twin activity. Such simulation results can assist in estimating the importance of the different elements which can control the twinning activity, like orientation, twin shape, even the effects of neighbour grains; these can be estimated from a direct comparison between simulation and experiment, grain by grain.

3. Material and methods

3.1. Initial material and experimental procedure

Hot-extruded Mg–3Al-0.3Mn alloy in the form of a rectangular bar was used as initial material. The initial microstructure was entirely devoid of twins and exhibited axisymmetric basal texture with the c-axis perpendicular to the extrusion direction (ED). It is well known that large grains promote the formation of twins during deformation in Mg alloys (Barnett et al., 2004; Jain et al., 2008; Ghaderi and Barnett, 2011). Thus, the material with larger grain size was employed so that the twining systems can be triggered easily. In this regard, quasi-static compression tests were performed along the extrusion direction (ED) on cuboidal shape samples, machined from the initial material as per ASTM standard E9-09 maintaining the height to width ratio equal to 1.5 with the dimensions: 4.5 mm × 4.5 mm x 6.75 mm, Teflon strips were introduced between the sample and the compression platens to minimize the barrelling effect caused due to friction. The tests were conducted using a computer-controlled servo-hydraulic 1344 Instron machine, at a low strain rate ($\dot{\varepsilon}$) of $= 7.4 \times 10^{-4}\ s^{-1}$ at ambient temperature until fracture and the load-displacement data were recorded. The obtained data were further analysed to plot the strain hardening curves. Further, the samples were also analysed at several intermittent strains to decipher the kinetics of twinning underlying the deformation mechanism.

3.2. Characterization

Comprehensive microstructural analysis was carried out using a field emission gun – scanning electron microscope (FEG-SEM), AURIGA Compact equipped with electron back-scattered diffraction (EBSD) camera. This characterization technique was adopted as it provided quantitative data regarding crystallographic texture, grain morphology and misorientations between pixels. Therefore, samples prior to and after deformation were subjected to characterization along the plane parallel to the compression direction. The samples were mechanically polished with ~4 μm roughness SiC paper followed by diamond polishing through a sequence of 1 μm and 0.25 μm to obtain a suitable examination surface. Subsequently, chemical polishing was carried out over a soft polishing cloth using a mixture of 83.33% methanol, 10% hydrochloric acid and 6.67% nitric acid (vol%) for 10 s to obtain mirror-like finish. Further, the surface was etched using a solution comprising of 5% nitric acid, 15% acetic acid, 20% distilled water and 60% ethanol (vol%) for 3–4 s to reveal the grain structures. This metallographic procedure ensured satisfactory indexing in the EBSD measurements. Scanning was performed over a large area ($1500 \times 1500\ \mu m^2$) at the centre of the sample surface to have statistically significant data. The indexing rate for the specimens was about 80–93%. Such a decline in indexing corresponds to the smearing of Kikuchi patterns due to the dislocation structures introduced with the increasing strain (Wright et al., 2011). The obtained orientation data were further processed using the non-commercial orientation imaging software ATEX (Beausir and Fundenberger, 2017).

3.3. Simulation procedure

3.3.1. Analysis conditions and identification of material parameters

The model presented in Section 2 was applied to simulate the mechanical response and the texture evolution while quantifying the evolution of twin variants for compression test. The boundary conditions corresponding to compression was imposed with true strain increments of $\Delta\epsilon = 0.01$. The input texture for the VPSC polycrystal code was constructed from the experimentally measured orientation data obtained from the EBSD scan of the initial material. In order to achieve this, the ATEX software (Beausir and Fundenberger, 2017) was used for discretizing the experimental ODF. The Euler space was discretized randomly to 12,000 orientations. For each orientation, the minimum misorientation angle with respect to all other orientations was computed. Then volume fraction was attributed to each orientation by integrating the ODF around the selected orientation within half of the minimum misorientation angle and are referred to as parent orientations. Thereafter, for each parent orientations, six extension twin orientations were assigned with zero initial volume fractions, created by rotating the parent orientations by 86.4° around the misorientation axes listed in Table 1. This constituted a total of $12{,}000 + (6 \times 12{,}000) = 84{,}000$ orientations. With this ATV modelling scheme, it was possible to keep track of the parent orientations and their respective six twin variants during the entire simulation.

Deformation was accomplished using the available slip and twinning systems of the HCP crystal structures according to previous works (Agnew et al., 2005b; Beausir et al., 2008; Biswas et al., 2010, 2013): basal $\langle a\rangle$ slip, prismatic $\langle a\rangle$ slip, first-order pyramidal $\langle c+a\rangle$ slip, second-order pyramidal $\langle c+a\rangle$ slip and $\{10\overline{1}2\}\langle 10\overline{1}\overline{1}\rangle$ extension twins (ET). Several simulation studies did not take into account the first-order pyramidal $\langle c+a\rangle$ slip in their approach (Graff et al., 2007; Choi et al., 2010; Ma et al., 2012; Zhang and Joshi, 2012; Cheng and Ghosh, 2015). However, recent studies suggest that the first-order pyramidal $\langle c+a\rangle$ slip should not be neglected (Beausir et al., 2008; Biswas et al., 2013; Fan and El-Awady, 2015; Fan et al., 2017; Xie et al., 2016; Srivastava and El-Awady, 2017). Hence, this slip system family was employed to address the real deformation behaviour properly. Further, the activation of each deformation mode was governed by its respective initial reference strength ($\tau_{0,i}$) in the VPSC code. For the strain rate sensitivity index, the value of $m = 0.1$ was selected for both slip and twinning as per the previous literature (Gu et al., 2013).

There are a total of 15 parameters that govern our modelling approach, see Tables 2 and 3. Our approach reproduces the strain hardening curve, twin volume fraction and texture evolution for definite values of these parameters that are presented in Tables 2 and 3 Several iterations were required to identify these parameters by comparing the simulated strain hardening curve, twin volume fraction and texture evolution with the experimental ones. Concerning the relative strengths of the slip systems, it has been found that among all families, the lowest strength had to be attributed to basal slip, in agreement with all previous investigations (Agnew et al., 2005b; Graff et al., 2007; Beausir et al., 2008; Biswas et al., 2010, 2013). The strength of the basal slip system was determined by fitting the initial slope of the simulated flow curve with the experimental measurement at the onset of plastic deformation. Thereafter, the strengths of other slip and extension twin systems were estimated in multiples of the CRSS of basal slip. An assessment on the relative strength of these deformation modes was achieved by comparing the simulated texture evolution and the twin volume fractions along with their experimental counterparts simultaneously. At the same time, the hardening coefficients for the parent and the twin grains were identified by capturing the sigmoidal shape flow curve from the simulation in agreement with the experimental measurement, see Table 3. Finally, the value of saturation stress in the hardening law was obtained when the simulated flow curve attained the experimental saturation stress.

4. Experimental and simulation results

In this section, both the experimental and simulated results are presented concerning strain hardening response, twinning activity and texture evolution.

4.1. Strain hardening response

The experimental flow curve, as well as the strain hardening rate ('SHR') plot obtained from the quasi-static compression test, is presented in Fig. 2a and b, respectively, in black lines. Correspondently, the simulated responses acquired from the presented model are shown using red lines. The triangular markers indicate the intermediate strain levels at ~0.05, ~0.08, ~0.10 and ~0.18, where the tests were interrupted for quantitative microscopy. The accuracy of the experimentally measured stress-strain response was ensured by testing at least three samples until failure, and the variance of these data was observed to be less than 4%. The compressive yield stress measured by the offset method ($e = 0.002$) was estimated to be ~72 MPa. The curve clearly depicts a sigmoidal shaped flow curve (Fig. 2a), thereby indicating profuse twin activities and the resultant increase in strain hardening rate (Agnew et al., 2001; Knezevic et al., 2010; Mu et al., 2011, 2014; Wang et al., 2012; Dixit et al., 2015). As can be seen in Fig. 2a, the simulation also reproduces a similar strain hardening behaviour in excellent agreement with the experimental flow curve after the onset of plastic strain. At the same time, the agreement for the SHR is also very good, see Fig. 2b. Deviations exist in the predicted curves at low strain regime because the elastic and elastic-plastic transitions were not modelled. Following incipient plasticity, the predicted curves exhibit a significant amount of strain hardening in Stage-II, which manifests a major contribution of twinning-mediated events to plasticity.

The SHR curve (Fig. 2b) can be used to divide the flow curve into three distinct stages: I, II and III. (Note that these stages are not the same as for cubic materials which deform by slip only. They are for hexagonal materials). Stage-I marks the initial stage of plastic strain through a sharp fall in SHR and is referred to as an elastic-plastic transition. Stage II follows this with an increase in SHR up to $\varepsilon \approx 0.10$. Thereafter, in Stage-III, a gradual drop in SHR occurs. Such mechanical behaviour corroborates well with previous experimental observations of Salem et al. (2003); Jiang et al. (2007b), Knezevic et al. (2010), Mu et al. (2011, 2014), Oppedal et al. (2012), Kabirian et al. (2015).

4.2. Texture evolution

Fig. 3a displays the experimental and simulated textures in terms of (0002) and $(10\bar{1}0)$ pole figures for the initial and the samples deformed to intermittent strains on the plane containing the compression direction (CD) and normal to one of the radial directions (RD). They were plotted without applying any sample symmetry. The orientation of the grains in the initial material can be characterized by a fibre type texture with two main components: one with a strong $\langle 11\bar{2}0\rangle||$CD with the intensity of $MRD_{max} \approx 17.92$ (MRD: Multiples of Random Distribution) but not fully continuous fibre, and the other with a weak $\langle 10\bar{1}0\rangle||$CD fibre. Together, these two components constitute the overall extrusion texture, as shown in Fig. 3a. After deformation to $\varepsilon \approx 0.05$, the crystal lattices reorient so that a basal-type fibre texture develops nearly parallel to the CD. At the same time, the intensity of the initial texture decreases dramatically to $MRD_{max} \approx 9.41$. Such rapid change in the texture is due to the reorientation of a portion of the matrix grains by ~86.4°, which corresponds to the rotational orientation relationship of $\{10\bar{1}2\}$ extension twinning. As deformation progresses, the original texture gradually diminishes and becomes weak at $\varepsilon \approx 0.10$. On the other hand, the intensity of the extension twin induced near-basal

Table 2
Initial material parameters used in the simulation for the slip and twin systems.

Slip/twin system	Basal	Prismatic	Pyramidal $\langle c+a\rangle$/I	Pyramidal $\langle c+a\rangle$/II	Extension Twin
Reference resolved shear stress (τ_0^s, MPa)	27	52	170	170	39

Table 3
Hardening parameters used for the parent matrix and the twin domains and the other modelling parameters, including twin aspect ratio and the interaction parameter.

Parameter	Value
Hardening coefficient for parent matrix, h_{matrix}	67 MPa
Hardening coefficient for twin domain, h_{twin}	1350 MPa
Saturation stress, τ_{sat}	267 MPa
Strain hardening parameter, a	0.4
Latent hardening parameters	$q_1 = 1$, $q_2 = 2$, $q_3 = 4$, $q_4 = 2$
Aspect ratio of twins	0.2 : 1: 1
Interaction parameter, α	0.1
Reference slip rate, $\dot{\gamma}_0$	0.001 s^{-1}

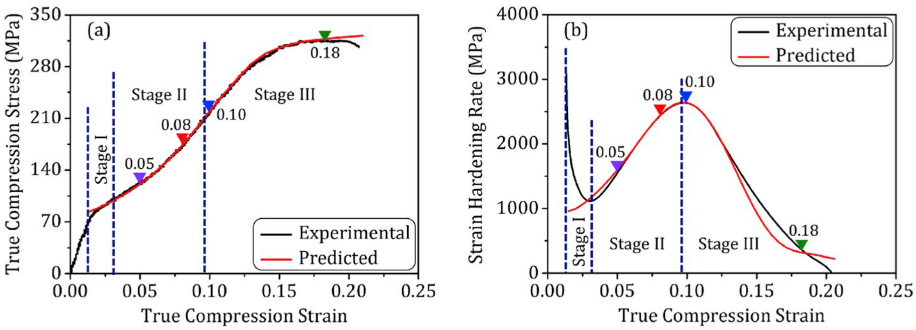

Fig. 2. Experimentally measured and predicted (a) true stress-strain response and (b) strain hardening rate behaviour of Mg–3Al-0.3Mn alloy tested in compression along the extrusion direction. The markers represent the intermediate strains at which the tests were interrupted for microstructural observations.

texture fibre gradually increases to MRD~17.50, at $\varepsilon \approx 0.18$. The predicted (0002) and $(10\overline{1}0)$ pole figures obtained from the present ATV approach matches the experimental texture quantitatively at every incremental strain. Besides, the model clearly predicts the gradual increase in MRD of the deformation texture with the strain (even the texture strength) and the formation of a near basal-type fibre texture, which can be attributed to the extension twins.

4.3. Microstructure evolution

Fig. 4a shows the evolution of the microstructure by means of inverse pole figure (IPF) maps on the CD-RD projection plane. Grains in these maps are outlined in black considering only high angle grain boundaries (HAGBs, larger than 15° misorientation). It can be seen that the initial microstructure comprises of slightly large elongated grains along the CD having an average grain size of ~108 μm (area-fraction weighted). The color code within the unit triangle represents the orientation of the sample radial direction (RD) within the hexagonal unit triangle. Mainly red and blue colored grains are seen which correspond to $\langle 0001\rangle||$RD and $\langle 2\overline{1}\overline{1}0\rangle||$RD orientations, respectively, thus, ensuring that the entire microstructure is favourably oriented for $\{10\overline{1}2\}$ extension twins during compression parallel to CD (Sahoo et al., 2019).

After a true compression strain, ε of ~0.05, the map clearly reveals the massive formation of thin lamellae/lenticular type morphology dominating the entire microstructure. These morphological features were identified as $\{10\overline{1}2\}\langle\overline{1}011\rangle$-extension twins having a rotational orientation relationship of ~86.4° about the $\langle 11\overline{2}0\rangle$ axis with respect to the surrounding parent matrix. Besides, these structures appear to be mainly green $\langle 10\overline{1}0\rangle||$RD and blue $\langle 2\overline{1}\overline{1}0\rangle||$RD colored, i.e., with entirely different orientations than the parent grains in the orientation maps (Fig. 4a). A detailed analysis demonstrates parallel colonisation of these structures in few grains with no intersection. While, in most grains, intersecting lamellar structures leading to the formation of ET-ET interface boundaries can be seen. These boundary features correspond to the activities and intersections of different twin variants. Concurrently, the broadening of these $\{10\overline{1}2\}$-extension twins can be observed in most of the grains, also at a $\varepsilon \approx 0.08$. Upon further deformation to $\varepsilon \approx 0.10$ and above, the initial orientations were almost wiped out by these entirely different orientations, thus, illustrating the domination of $\{10\overline{1}2\}$-extension twinning. As a result, the experimental evidence stipulates that the extension twins grow in size and encompass the entire parent microstructure leaving a meagre volume fraction of the parent matrix in their initial orientation. The decrease in the average grain size to ~46.92 μm, due to the formation of extension twins at $\varepsilon = 0.05$ can be observed in Fig. 4a. However, at a later stage, broadening of the extension twins led to an increase in the average grain size to ~73.5 μm at $\varepsilon \approx 0.18$. In fact, previous works on Mg alloys (Knezevic et al., 2010; Dudamell et al., 2011; Dixit et al., 2015; Molodov et al., 2017) have also indicated similar growth behaviour of $\{10\overline{1}2\}$-extension twins during deformation. It is important to note here that in all these cases, no secondary twinning was found.

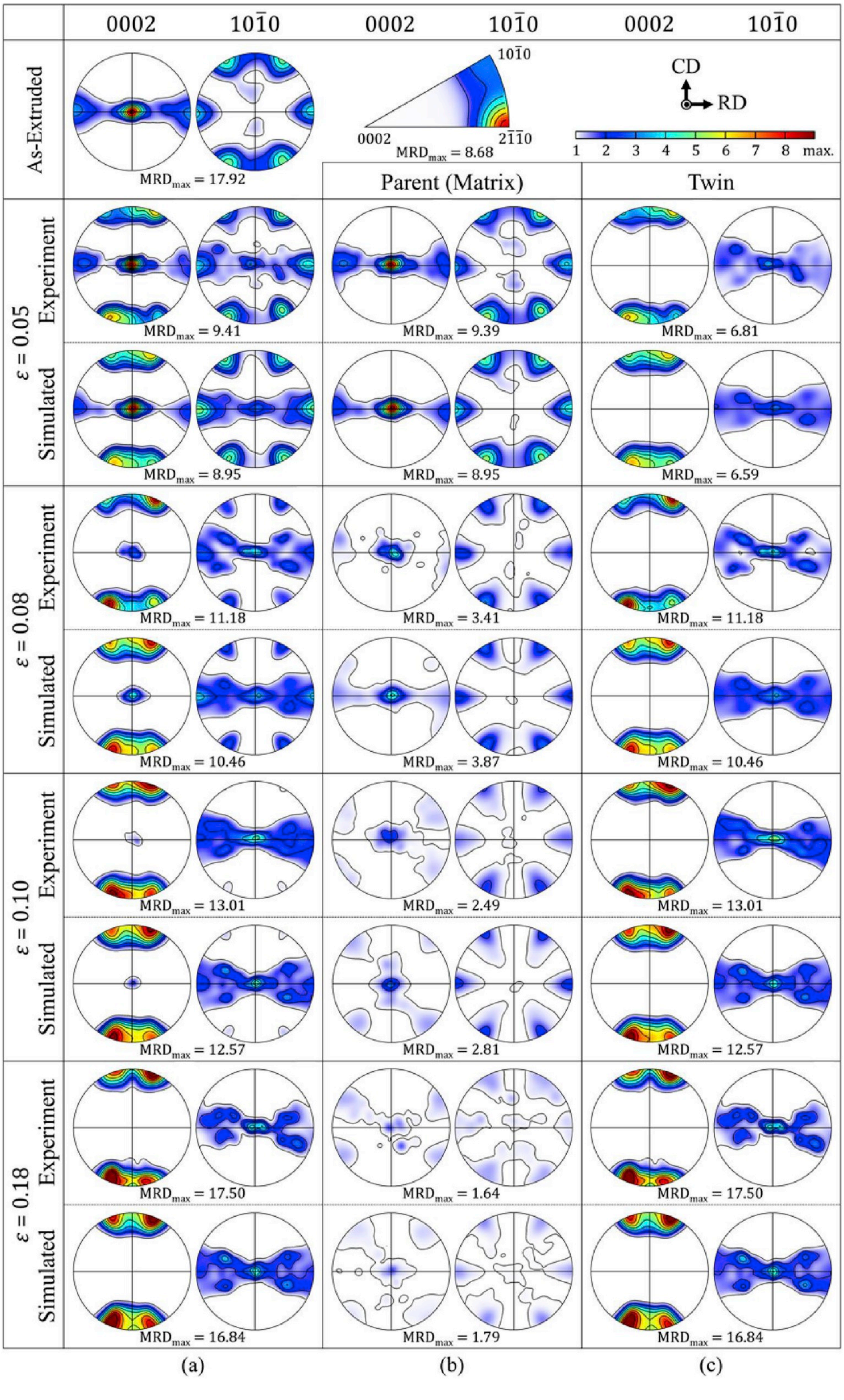

(caption on next page)

Fig. 3. Experimentally obtained texture for the initial as-extruded Mg–3Al-0.3Mn alloy is represented by (0002) and $(10\bar{1}0)$ pole figures, and inverse pole figure for the compression direction. Experimentally measured and predicted (0002) and $(10\bar{1}0)$ pole figures for the Mg–3Al-0.3Mn alloy with increasing strain depicting (a) the overall texture, (b) the texture derived from the parent matrix and (c) the texture obtained from the twin domains. The color scale represents multiples of random distribution. (For interpretation of the references to color in this figure legend, the reader is referred to the Web version of this article.)

4.4. Evolution of misorientation angles due to extension twin boundaries

In order to further understand these extension twin structures, misorientation angle (θ) distribution for the as-received, as well as the samples deformed to intermediate strains were plotted in Fig. 5. At first, the grains were identified in the maps with the minimum misorientation of 5° across their boundaries, and then their average orientations were calculated by integrating the pixel-quaternions within the grains to obtain θ (Beausir and Fundenberger, 2017). θ refers to the smallest orientation difference between the average orientations of neighbouring grains, which brings an orientation in coincidence with the orientation of its neighbour. Such kind of grain-to-grain misorientation angle distribution was introduced by Toth et al. (2010), which is suitable for studying orientation correlations in deformed polycrystals. The initial microstructure (shown in Fig. 5a) exhibited a diffused distribution of peaks at all misorientation angles, near to the misorientation curve that corresponds to the random misorientation distribution for hexagonal polycrystals.

At a strain of ~0.05 (Fig. 5c–i), the misorientation angle distribution histogram portrays a high peak at ~86.4± 4°, and three modest rises at ~60±3°, ~30±2° and ~7.4±1°. The misorientation angle-axis pair pertaining to the $\{10\bar{1}2\}$ extension twins and for different ET-ET configurations are summarized in Fig. 5b (Nave and Barnett, 2004; Jiang et al., 2008; Park et al., 2010). The large increase in ~86.4° misorientation angle is attributed to the evolution of numerous extension twin boundaries. This can be observed from the angular inverse pole figure in Fig. 5c–i to 5f-i constructed for 86.4° misorientation about the $\langle 11\bar{2}0\rangle$ axes. At the same time, the ~60° misorientation angle forms owing to the intersection of two different extension twin variants. The angular inverse pole figure of the same is displayed in Fig. 5c–i to 5f-i, which indicates a strong intensity for the rotation relationship about the $\langle 10\bar{1}0\rangle$ axes and is related to the intersection between $(10\bar{1}2)-(01\bar{1}2)$ twin variants (See Table 1 for twin variants). On the other hand, another rotation orientation relationship of ~60.4° about $\langle 8\bar{1}\bar{7}0\rangle$ axes also occur due to $(10\bar{1}2)-(0\bar{1}12)$ twin intersection, see Fig. 5b. However, this case could not be detected in the IPF maps. A small but diffused peak at ~7.4° that may correspond to the interaction of the same twin variant pair leading to the formation of low angle symmetrical tilt boundaries about $\langle 11\bar{2}0\rangle$ axes could also form (Hu and Randle, 2007; Bozzolo et al., 2010; Zhang et al., 2017). Additionally, all the misorientation angle distributions show the presence of a peak at 30° associated with the static/dynamic recrystallization in Mg alloys (Nadella et al., 2003; Ulacia et al., 2010; Al-Samman et al., 2012; Biswas et al., 2015a,b; 2018). From the geometrical point of view, the 30° misorientation angle peak occurs due to the rotation of orientations along [0001] and is associated with Σ13*a* coincident site lattice (CSL) boundaries (Ostapovets et al., 2011, 2012) possessing low energy configuration (Zhu et al., 2009). This is mainly attributed to the presence of both deformed $\langle 2\bar{1}\bar{1}0\rangle$||ED and recrystallized $\langle 10\bar{1}0\rangle$||ED orientations commonly observed in extruded Mg alloys (Yi et al., 2010; Martin et al., 2010; Mayama et al., 2011; Al-Samman et al., 2012).

As the strain increases (Fig. 5d–i to 5f-i), a decline in the intensity of the ~86.4° misorientation peak is observed with a gradual spread. This is counterbalanced by a slight increase and broadening in the ~60° peak whereas the fraction of ~7.4° misorientation angle remains low throughout the deformation up to fracture. The appearance of broadening indicates a gradual shift in the misorientation (Mokdad et al., 2017). Indeed, the twin induced misorientation angles changed during further plastic deformation because the lattice rotation within the twins were different from the matrix rotation. This is due to the differences in the activated slip systems in the parent matrix, and the twin domains owing to their orientation difference discussed later in section 4.5.

The present modelling permits to calculate misorientations between the given parent grain and its twin variants, and also between its own twin variants. By doing so for all the parent grains, a misorientation distribution can be obtained on the polycrystal. Note that the VPSC approach cannot calculate misorientations between neighbour parent grains, as there is no direct neighbouring in the modelling. Nevertheless, it is useful to examine the 'internal' misorientation distribution obtained from the inside of the parent grains. The so-obtained simulated misorientation angle distributions are displayed in Fig. 5c–ii to 5f-ii. The model could capture the high fraction of ~86.4° and the modest fractions of ~60° and ~7.4° misorientation angles with a certain spread for all intermittent strains. Recent studies on extension twins in Mg alloys (Ostapovets et al., 2011, 2012) indicated that the intersection between any two variants of twin results in the formation of CSL boundaries. The 86.4° extension twin tilt boundaries about $\langle 11\bar{2}0\rangle$ axes are associated with Σ15*b* boundaries. Similarly, the appearance of 60° tilt boundaries about $\langle 10\bar{1}0\rangle$ due to the intersection of two extension twin variants of different pairs are associated with Σ31*b* CSL boundaries. It can be observed that the predicted misorientation angles acquired by the present ATV approach are in good correlation with the experimental counterparts. At low strain ($\varepsilon = \sim 0.05$), a large fraction of Σ15*b* and a moderate fraction of Σ31*b* boundaries develop. As plastic deformation progresses, the growth behaviour of the twin variants can be rationalized in the light of their morphological evolution leading to the formation of Σ15*b* CSL boundaries. A gradual decline in the number fraction of Σ15*b* (86.4°) boundaries with increasing strain is due to dislocation slip within the twin domains. In general, this behaviour is a consequence of the difference in lattice rotation between the twin and the parent grains, which gradually accumulates during deformation and eventually fails to maintain the exact twin misorientation (This is explained in detail in section 4.5). Due to this phenomenon, misorientations at the left side of the 86.4° that appears in the simulated distribution, progressively extend towards the 60° peak (Fig. 5c–ii to 5f-ii). This effect reduces the number of near-exact misoriented twins, leading to a decrease in their

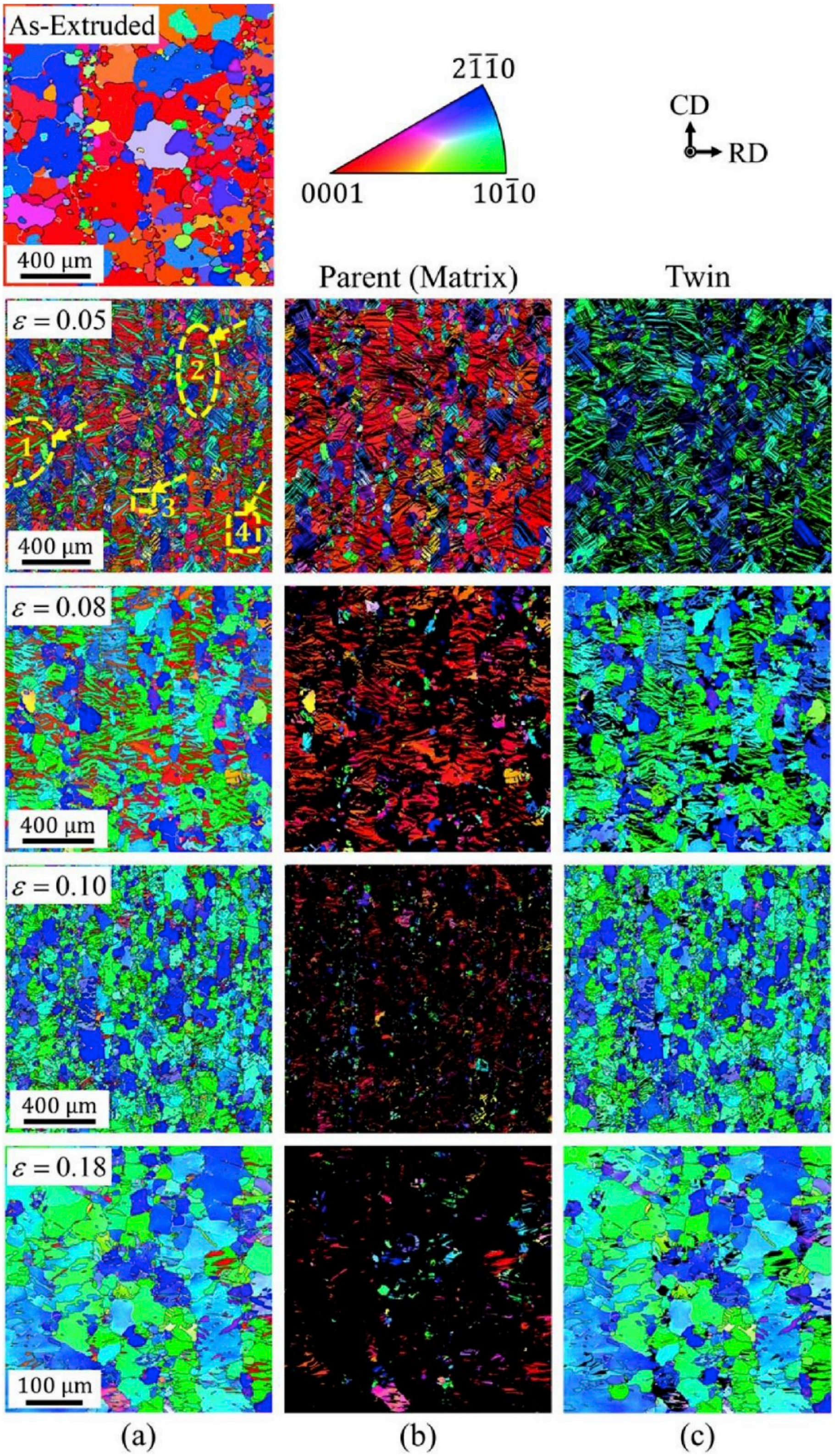

Fig. 4. Inverse pole figure maps of the initial, as well as the compression, tested Mg–3Al-0.3Mn alloy at different strain levels on the CD-RD plane: (a) the entire microstructure, (b) the parent matrix and (c) the twin domains. The color code corresponds to the projection of the RD direction. (For interpretation of the references to color in this figure legend, the reader is referred to the Web version of this article.)

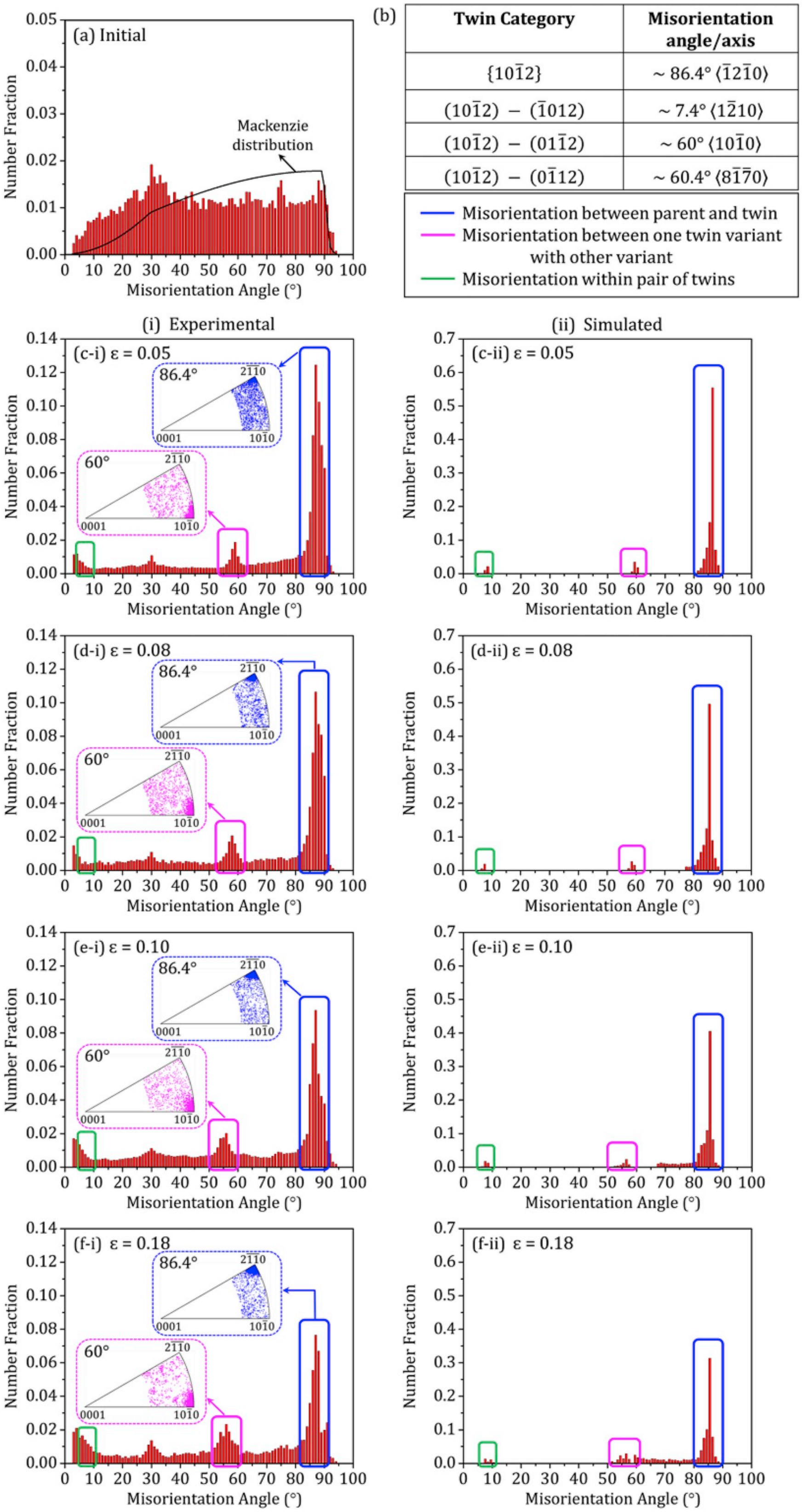

(caption on next page)

Fig. 5. (a) The misorientation angle distribution histogram of the as-extruded shown vis-à-vis the Mackenzie distribution plot; (b) The most frequently observed twin types in Mg alloys along with their corresponding misorientation angle/axis pairs; (c–f) Experimental and Predicted misorientation angle distribution histogram at intermediate strains along with the experimental misorientation angle/axis inverse pole figures.

frequency.

Further, it should be noted, that the number fraction of the predicted misorientation angle distribution was much higher (Fig. 5c–ii to f-ii) than the experimentally measured ones (Fig. 5c–i to f-i) for incremental strain. This is because there were no direct neighbour parent grains in the simulation, while many twins in adjacent grains have common boundaries in the experiment.

4.5. *Predicting the activities of slip and twin systems*

The accurate prediction of the three-stage strain hardening response and the texture evolution assists in determining the contribution of deformation modes with strain. The current approach relies on the fact that the response of the polycrystal to plastic deformation is driven by both the parent matrix and corresponding twin variants. Plasticity in the twin is mediated by considering it as a grain while allowing only slip inside it, i.e., no twinning within twin-grains. Fig. 6a and b illustrate the relative activities of slip and twin system families obtained from our VPSC simulations as a function of strain. Here, the activities were calculated as the ratio of the sum of the strain rates in the slip systems of a given family to the total slip rate in the grains (absolute values were used). The same was applied for the twinning systems while considering them as pseudo-slips in the parent grains.

In the parent matrix (Fig. 6a), the activities of extension twins were found to be the highest initially, which decreased progressively with strain. This is in accordance with the experimental investigation (Fig. 4a, $\varepsilon \approx 0.05$) that indicates profuse twinning at early strains. Beyond $\varepsilon \approx 0.10$, the entire microstructure is almost engulfed by extension twin, and a small fraction of parent matrix remains. Concerning the slip systems within the parent matrix, the prismatic slip showed the highest activity for the parent matrix. This is a consequence of the initial texture. Though the basal slip system family had the lowest strength, its activity was initially low compared to prismatic slip. This is due to the unfavourable orientation of basal slip in the parent grains. Several studies reported the same during deformation of Mg alloys at lower temperatures (Agnew et al., 2003, 2005; Keshavarz and Barnett, 2006; Ulacia et al., 2010; Mayama et al., 2011). However, as the parent grains were not in ideal orientation with respect to compression, they rotated significantly upon progressive straining. This can also be evidenced by the pole figures of the parent-grain population plotted from the simulation, as shown in Fig. 3b. A detailed analysis of the (0002) pole figures of the parent grains thereby suggests that the remaining parts of the parent grains progressively oriented with their c-axis towards the 45° position with respect to the CD axis. In that position, the basal slip is ideally oriented for compression, and hence further deformation might be preferentially favoured by basal slip. This is precisely the case in the slip system activity of the parent grains in Fig. 6a, which indicates that the basal slip becomes the most active

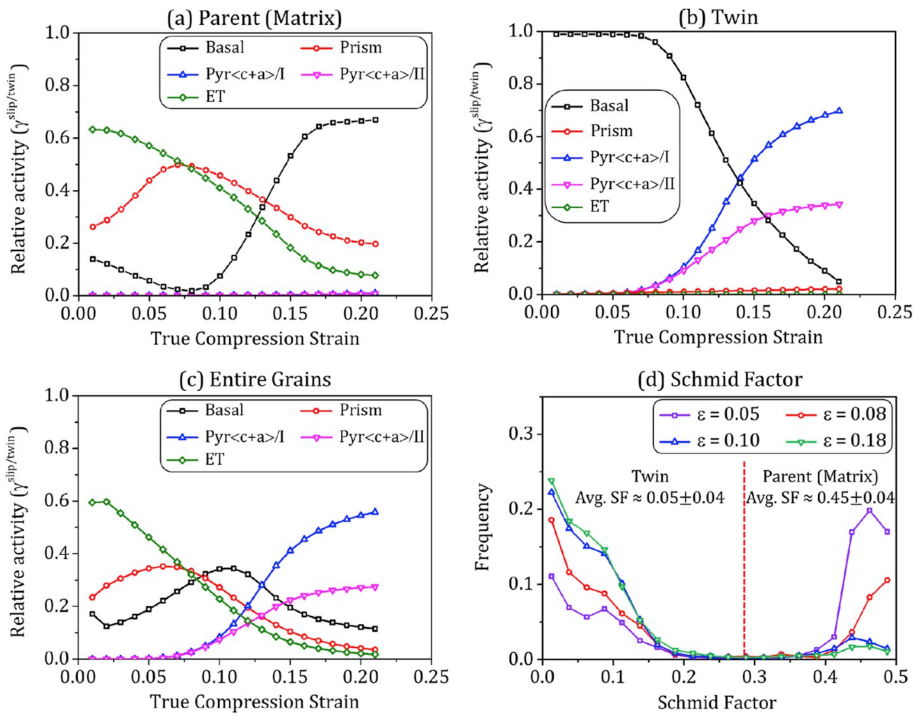

Fig. 6. Activities of various slip and extension twin deformation modes predicted by the ATV approach as a function of true compressive strain for the (a) parent matrix, (b) twin domains, (c) entire microstructure; (d) the prismatic slip Schmid factor plot with respect to the frequency of grains.

commencing from $\varepsilon \approx 0.11$. The pyramidal slip activities were found to be negligible throughout the deformation in the parent grains.

In the case of twin-grains (Fig. 6b), increased activity of basal slip could be observed at lower strains that gradually declined from $\varepsilon \approx 0.10$ to nearly zero at $\varepsilon \approx 0.20$. The activities of the prismatic slip and extension twins were found negligible throughout the strain. However, significant activities of pyramidal $\langle c+a\rangle$/I and $\langle c+a\rangle$/II could be observed after $\varepsilon \approx 0.10$. The increase in the activities of the pyramidal $\langle c+a\rangle$ type slip system in the twin domains is reported and explained in several studies (Obara et al., 1973; Morozumi et al., 1976; Agnew et al., 2002; Dixit et al., 2015; Wang and Agnew, 2016; Fan and El-Awady, 2017, 2017; Xie et al., 2016; Srivastava and El-Awady, 2017). Further, it can be noticed that among the pyramidal $\langle c+a\rangle$ type slip system, the pyramidal $\langle c+a\rangle$/I slip contributes more towards plastic slip as compared to that of pyramidal $\langle c+a\rangle$/II slip.

Subsequently, the activities of the deformation modes for the entire polycrystal was obtained from the activities of slip and twin systems in the parent matrix and twin domains (Fig. 6a and b, respectively) and shown in Fig. 6c. It can be observed that below $\varepsilon \approx 0.10$, where the microstructure contained mostly parent grains, the most active slip system is the prismatic $\langle a\rangle$ type slip system. Beyond $\varepsilon \approx 0.10$, the microstructure was dominated mostly by twins, therefore Fig. 6c indicates mostly the slip and twin activities within the twin domains.

4.6. Partitioning of the experimental microstructure and texture

The above analysis illustrates that prismatic slip is the most active within the parent matrix and inactive within the twin domains. Such discrepancy in the activities of prismatic $\langle a\rangle$ slip system within the parent matrix and the twin domain is originating from the difference in their orientation. In order to confirm the above proposition and to further substantiate this through our experimental work, a Schmid factor (SF) analysis of prismatic $\langle a\rangle$ slip system for these two domains was conducted. The frequency of the Schmid factor of the prismatic slip was calculated for all intermittent strain conditions for the entire microstructure, see Fig. 6d. It can be clearly seen that the plot is distinctive with the presence of minima dividing the microstructure into two regions. One region is with an average SF $\approx 0.45 \pm 0.04$, and another is with an average SF $\approx 0.05 \pm 0.04$. The high SF indicates the most active prismatic slip region, which represents the parent matrix. While the low SF region possesses no prismatic activity and therefore considered as twin domains. Hence, the microstructure pertaining to all the intermittent strains shown in Fig. 4a could be partitioned using the prismatic Schmid Factor criteria into the matrix and twin domains. Fig. 4b shows the high SF regions in which the parent matrix is colored red for $\langle 11\overline{2}0\rangle||$CD and blue for $\langle 10\overline{1}0\rangle||$CD grains (with c-axes nearly perpendicular to CD, as discussed in Section 4.3). It can be seen from Fig. 4b that the fraction of these grains diminishes with strain. Whereas, Fig. 4c shows the low prismatic-SF twinned regions that contain mostly green $(10\overline{1}0)||$RD and blue $(11\overline{2}0)||$RD grains (with c-axes nearly parallel to CD). These twin domains gradually evolve with deformation.

Fig. 3b and c displays the respective texture of the partitioned parent and twin domains in the form of (0002) and $(10\overline{1}0)$ pole figures. In particular, the partitioned parent matrix exhibited $\langle 11\overline{2}0\rangle$ and $\langle 10\overline{1}0\rangle$ prismatic fibre textures up to the strain of $\varepsilon \approx 0.08$. Further, it is important to note that the maximum MRD of the fibre gradually diminishes with the increase in strain. On the contrary, the (0002) and $(10\overline{1}0)$ pole figures for the partitioned twinned domains exemplify four near basal texture components towards the compression direction and are attributed to the extension twins. The gradual evolution of these components could also be visually observed with strain. This is analogous to the computed texture obtained by partitioning the parent and the twin orientations in the simulation, as shown in Fig. 3b and c, respectively. The results show that upon increasing strain, the predicted texture of the parent matrix diminishes, while the components corresponding to the twin variants gradually strengthen. This signifies the predictive capability of the model that itself is governed by the activation of twin variants by virtue of their respective volume fraction evolution with strain. The corroboration of the partitioned experimental textures with the simulated ones clearly indicates a realistic partitioning of the microstructure.

It is also interesting to analyse the misorientation angle distributions separately for the two partitioned microstructures. They were plotted by considering only neighbouring grains with common boundaries, i.e. the misorientation between parent grains in the matrix microstructure and between the twin variants for twins. The so-obtained plots are presented in Fig. 7 for all intermittent strains. For the

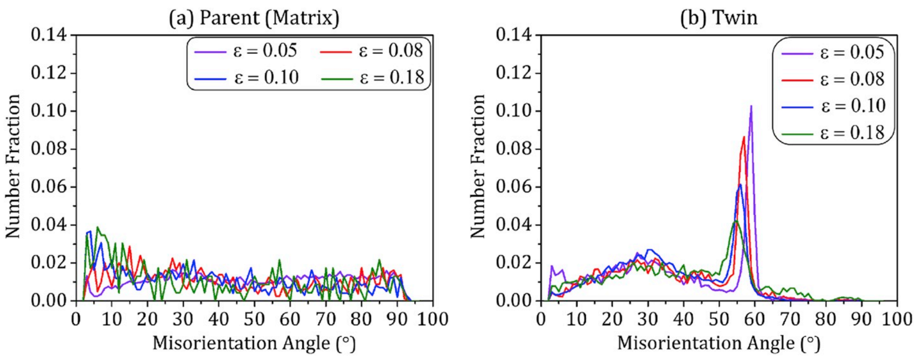

Fig. 7. Misorientation angle distribution plot for the (a) parent matrix and (b) twin domains.

parent grains (Fig. 7a), a diffuse distribution is obtained with no preference for specific misorientation values irrespective of the strain levels. This result is related to the initial texture, which already showed similar misorientation distribution (Fig. 5a). On the contrary, the misorientation angle distribution plot for the twin-grains (Fig. 7b) shows high preference at ~60° misorientation along with a modest preference at a misorientation of ~30°. This clearly manifests the existence of two cases which appear at the same time, owing to (i) intersections of different variants within the same initial parent grain, and (ii) misorientations between twins of neighbouring parent grains. In particular, the origin of the ~30° peak is certainly for the latter configuration, while the ~60° large peak is originating due to the intersection between different twin variants within the same parent grain. Indeed, the existence of ~60° misorientation is more frequent for the same hexagonal crystal during profound twinning, see the Table inserted into Fig. 5b. As deformation continues, this large peak in the twin-grain (Fig. 7b) gradually decreases and broadens, which can be attributed to the different lattice rotations of the intersecting twin-grains. This implies that they naturally rotate to different directions producing a large orientation difference. As a consequence, it clearly depicts the presence of different slip system activity within them. Furthermore, the absence of the ~86.4° misorientation in the twin-grain misorientation distribution is natural as this angle is between a twin-variant and matrix, and the matrix grains are not part of the twin-grain partitioned microstructure. Hence, it is of utmost important to mention that the absence of the ~86.4°, ~60° and ~7.4° peaks in the partitioned parent matrix also confirms the successful partitioning of the microstructure again into the representative parent matrix and twin domains using the prismatic Schmid-factor principles presented in Section 4.6.

4.7. Quantitative determination of the total twin volume fraction

In order to corroborate the quantitative prediction of twin volume fraction obtained from the ATV approach with the experimental counterpart, the occupancy of the twins from the entire microstructure was quantified for the intermediate strains through the prismatic Schmid factor-based partitioning procedure as discussed in Section 4.6. Such analysis quantitatively determines the area fraction of extension twin domains (Fig. 4c) in the entire microstructure for all intermediate strains. The so-obtained twin area fraction derived from the two-dimensional EBSD maps has been considered equivalent to twin volume fraction for the entire specimen (Mason et al., 2002; Ghaderi and Barnett, 2011; Pei et al., 2012). The experimentally determined volume fraction of extension twin domains obtained from the above partitioning method is plotted with a black dashed line as a function of strain in Fig. 8a. The cumulative volume fraction of the simulated extension twin variants (shown in solid red line) is also plotted vis-à-vis the experimental results in the same figure. It can be seen that the model accurately predicts the volume fraction of the extension twins, in agreement with the experimental measurements.

In order to have an insight into the contribution of the six extension twin variants, their respective volume fraction predicted from the simulation is presented in Fig. 8b for four strain levels. As can be seen in this figure, four variants are very active, and two are practically negligible. The origin of this particular result is the strong initial crystallographic texture and will be explained in the Discussion part.

4.8. Twin variants in individual grains

In this section, it is demonstrated that the present approach is not only reproducing the average properties satisfactorily (texture, strain hardening and twin volume fraction) but also applicable for analysis on individual grain basis. This capacity of the present modelling is the key novelty since such successful quantitative analysis was never achieved in prior modelling studies using the VPSC polycrystal model with twinning. In general, the VPSC approach is a homogenisation scheme designed for modelling average properties, rarely used for predicting the behaviour of individual grains.

To examine the ability of this modelling approach on individual grains, one should know the orientation of the selected parent grain in the initial as well as in the final state, together with the operating twinning systems. However, the present modelling was not

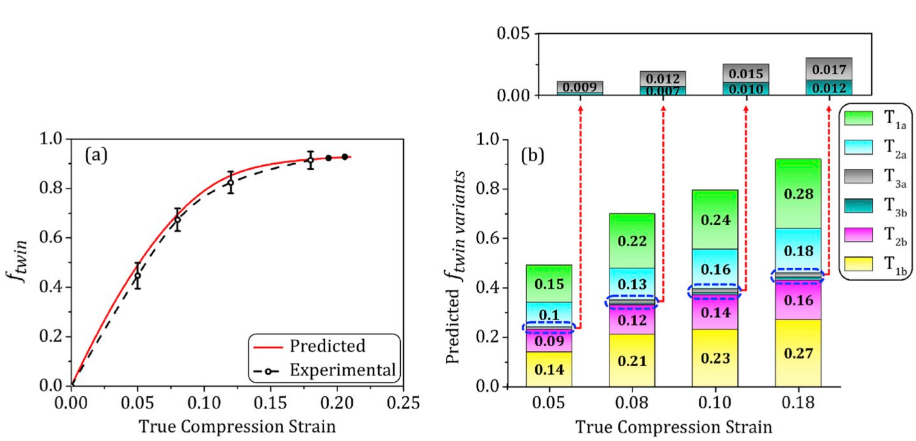

Fig. 8. (a): Comparison between the EBSD measured and predicted extension twin volume fraction as a function of true compression strain. (b): Predicted evolution of the volume fractions of the six extension twin variants.

performed in this manner; as experimentally, the investigation could only be carried out at the final state and not on the initial one for the same material volume. Nevertheless, the examined surface was within the bulk of the sample, and the sample was sectioned for analysis *after* deformation. The EBSD-IPF maps show the microstructure that was obtained within the bulk and not on the surface area. Therefore, the VPSC modelling conditions were fully satisfied for our observed microstructures as the grains were really 3D inclusions within the polycrystal. In order to access the initial orientation of the parent grain, the following simulation procedure was adopted. At first, the orientation distribution function of the initial texture was generated from the measured EBSD maps for the initial state. For this purpose, a large number of grains (12,000 parent orientations) were used with appropriate volume fractions to reproduce the initial texture. As explained already in Section 3.3.1, each of these parent grain orientation was complemented with six other twin-grain orientations; thereafter, the VPSC simulation was carried out. After completion of the simulation work, the orientation of the 45 randomly selected individual parents' grains $(\phi_1, \varphi, \phi_2)$ were obtained from the experimentally measured EBSD-IPF map corresponding to $\epsilon = 0.05$. The nearest possible parent orientations were traced from the simulated $(\phi_1, \varphi, \phi_2)$ output list with a tolerance of $\pm 2^\circ$. Finally, the simulation results obtained for the parent and corresponding twin phases were compared to the experiment.

4.8.1. Detailed analysis for four selected grains

Four of the 45 grains were selected (shown in Fig. 4a) for detailed analysis, and are referred to as grains 1, 2, 3 and 4. These grains were cropped from Fig. 4a ($\epsilon = 0.05$) and shown at higher magnification in Figs. 9a, 10a, 11a, and 12a. Visual inspection indicates that these grains are profoundly twinned and the extension twins in these grains can be readily recognized from their morphological characteristics along with their notable change in orientation. Grains 1 and 2 exhibits twin structures intersecting with each other, while grains 3 and 4 possess parallel-twin morphology. They differ in their initial crystallographic orientations with respect to the CD axis, i.e., grains 1 and 2 are oriented nearly $\langle 11\bar{2}0\rangle||$CD, while 3 and 4 are close to $\langle 10\bar{1}0\rangle||$CD.

Grains 1 and 2 in Figs. 9a and 10a portray lenticular structured extension twins intersecting with each other. Correspondingly, their respective pole figures display four reflections ~30° away from the CD (Figs. 9b and 10b). Thus, it suggests that multiple twin variants were active in these parent grains during deformation. The corresponding parent grain orientation was identified from the output orientations of the simulation. The predicted (0002) and $(10\bar{1}0)$ pole figures were plotted using the parent orientation along with its six

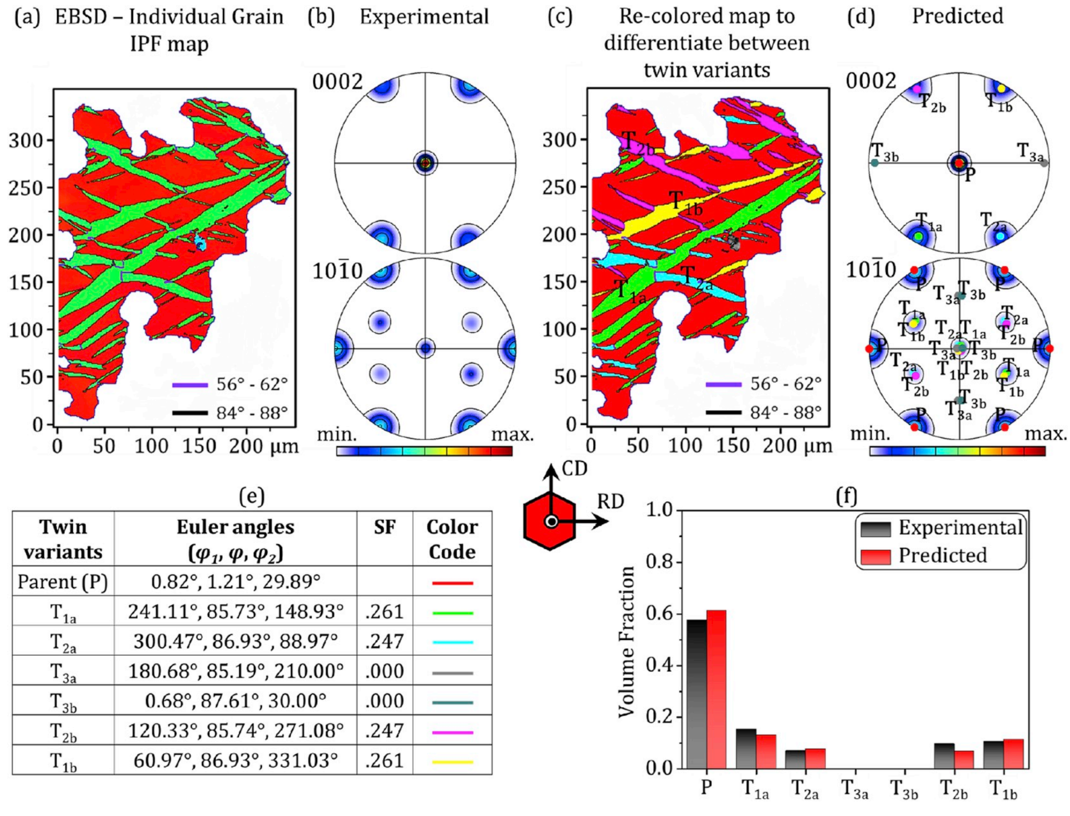

Twin variants	Euler angles $(\varphi_1, \varphi, \varphi_2)$	SF	Color Code
Parent (P)	0.82°, 1.21°, 29.89°		red
T_{1a}	241.11°, 85.73°, 148.93°	.261	green
T_{2a}	300.47°, 86.93°, 88.97°	.247	cyan
T_{3a}	180.68°, 85.19°, 210.00°	.000	grey
T_{3b}	0.68°, 87.61°, 30.00°	.000	dark teal
T_{2b}	120.33°, 85.74°, 271.08°	.247	magenta
T_{1b}	60.97°, 86.93°, 331.03°	.261	yellow

Fig. 9. (a) Inverse pole figure map of Grain 1 with CD $\|\ \tilde{}\langle 11\bar{2}0\rangle$ (the parent orientation is represented by the HCP unit cell with reference directions, CD and RD), (b) its corresponding (0002) and $(10\bar{1}0)$ pole figures, (c) Re-colored map showing twin variants in distinctive color plotted with respect to their predicted Euler angles, (d) Predicted (0002) and $(10\bar{1}0)$ pole figures, (e) Table summarizing the Euler angles of the corresponding parent and the predicted twin variants with their respective Schmid factor and color code for Fig. 9c, (f) Measured and predicted volume fraction of the parent grain and the twin variants. (For interpretation of the references to color in this figure legend, the reader is referred to the Web version of this article.)

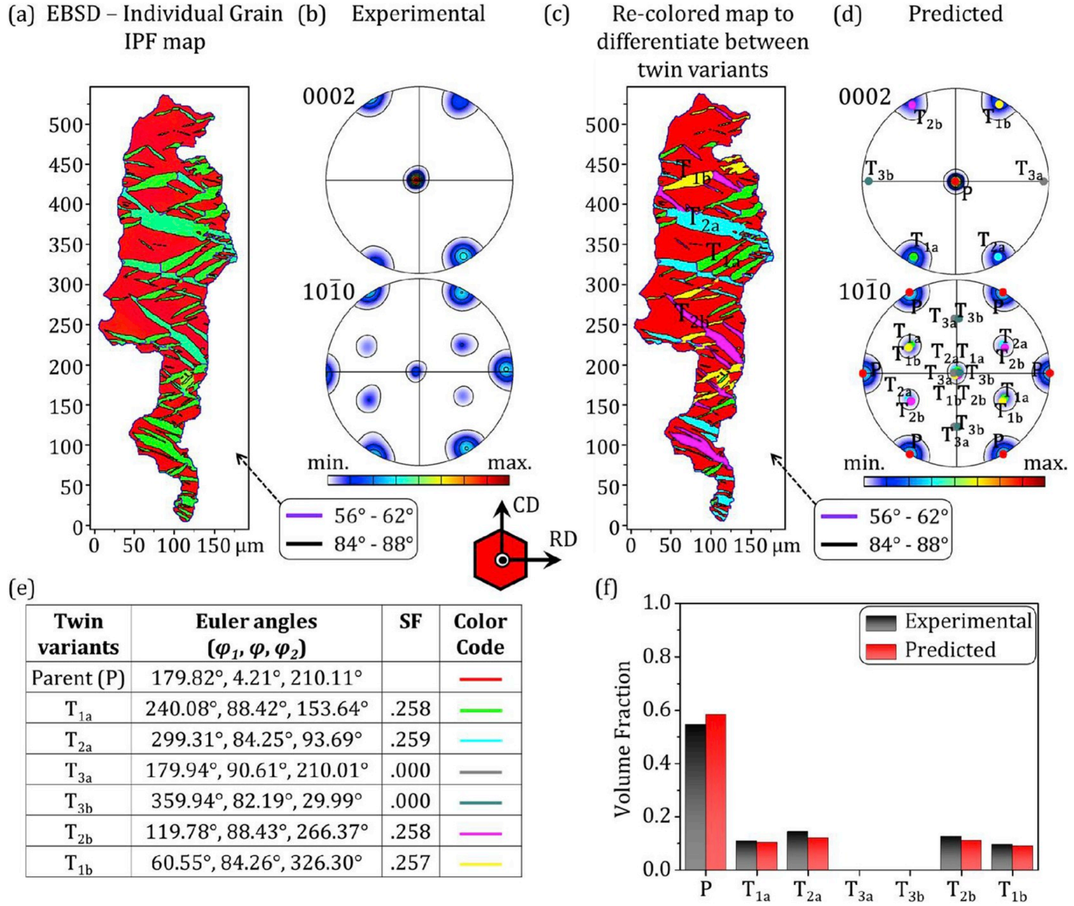

Twin variants	Euler angles ($\varphi_1, \varphi, \varphi_2$)	SF	Color Code
Parent (P)	179.82°, 4.21°, 210.11°		red
T_{1a}	240.08°, 88.42°, 153.64°	.258	green
T_{2a}	299.31°, 84.25°, 93.69°	.259	cyan
T_{3a}	179.94°, 90.61°, 210.01°	.000	grey
T_{3b}	359.94°, 82.19°, 29.99°	.000	teal
T_{2b}	119.78°, 88.43°, 266.37°	.258	magenta
T_{1b}	60.55°, 84.26°, 326.30°	.257	yellow

Fig. 10. (a) Inverse pole figure map of Grain 2 with CD ‖ ~⟨11$\bar{2}$0⟩ (the parent orientation is represented by the HCP unit cell with reference directions, CD and RD), (b) its corresponding (0002) and (10$\bar{1}$0) pole figures, (c) Re-colored map showing twin variants in distinctive color plotted with respect to their predicted Euler angles, (d) Predicted (0002) and (10$\bar{1}$0) pole figures, (e) Table summarizing the Euler angles of the corresponding parent and the predicted twin variants with their respective Schmid factor and color code for Fig. 10c, (f) Measured and predicted volume fraction of the parent grain and the twin variants. (For interpretation of the references to color in this figure legend, the reader is referred to the Web version of this article.)

twin variants, by taking into account their volume fractions. Figs. 9e and 10e display the Euler angles of the parent orientations for grains 1 and 2, respectively, together with the corresponding six possible predicted extension twin variants. It can be seen in the pole figures that the measured and predicted positions of the twins are coinciding with each other. This is expected, as the same parent orientation was selected from the simulation as the experiment. However, it was not evident that good agreements will be achieved in terms of their intensities. The measured and predicted parent and twin volume fractions are presented in the form of a histogram in Figs. 9f and 10f. Again, good agreements can be noticed between simulation and measurement. Finally, a new procedure was adopted to find out the individual twin variants within the microstructure. Indeed, all twin variants in the EBSD image appear nearly with the same color, while they have different orientations. This happens because, in an IPF, all orientations that are rotated around the projected sample axis are colored the same. Therefore, to clearly observe the different twin variants, the twins were re-colored according to their variants using the simulation result. Different colors were attributed to each variant (see the color code in Figs. 9e and 10e) and the corresponding twins in the microstructure (Figs. 9c and 10c) were colored accordingly (using 3.5° orientation tolerance angle). This was made possible with the help of the ATEX orientation software developed by Beausir and Fundenberger (2017), which was modified for this purpose. As can be seen, the twin microstructure becomes more informative by providing precise information on the different twin variants.

Conversely, Grains 3 and 4 in Figs. 11a and 12a initially possess ⟨10$\bar{1}$0⟩||CD orientation, as shown by the (0002) and (10$\bar{1}$0) experimental pole figures (Figs. 11b and 12b). In these conditions, only parallel colonies of extension twins appeared. The simulated pole figure for the same also reflects an identical projection for the twin variants (as shown in Figs. 11d and 12d), in agreement with the experimental measurements. Correspondingly, the Euler angles for the parent and twin variants are illustrated in Figs. 11e and 12e. It is interesting to note that for both grains nearly parallel-twin lamellas appear in the EBSD map, while they actually correspond to different variants, shown by the re-colored microstructure maps in Figs. 11c and 12c. The experimental and simulated volume fractions

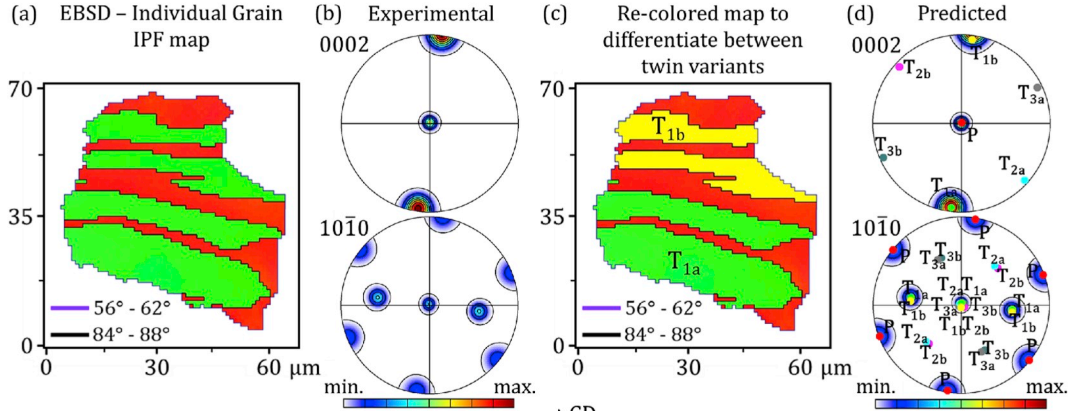

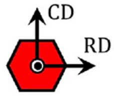

(e)

Twin variants	Euler angles (φ_1, φ, φ_2)	SF	Color Code
Parent (P)	346.19°, 1.02°, 63.63°		red
T_{1a}	260.07°, 86.41°, 148.99°	.344	green
T_{2a}	319.72°, 87.31°, 89.61°	.144	cyan
T_{3a}	20.24°, 87.24°, 30.53°	.040	grey
T_{3b}	200.31°, 85.55°, 209.40°	.039	dark teal
T_{2b}	139.66°, 85.49°, 270.53°	.132	magenta
T_{1b}	79.94°, 86.27°, 331.03°	.331	yellow

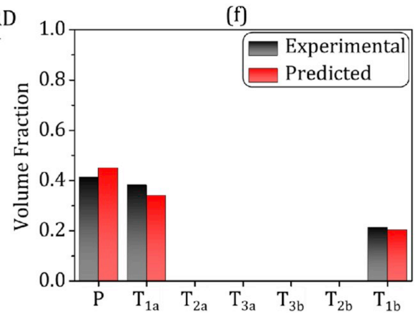

Fig. 11. (a) Inverse pole figure map of Grain 3 with CD ∥ ~⟨10$\bar{1}$0⟩ (the parent orientation is represented by the HCP unit cell with reference directions, CD and RD), (b) its corresponding (0002) and (10$\bar{1}$0) pole figures, (c) Re-colored map showing twin variants in distinctive color plotted with respect to their predicted Euler angles, (d) Predicted (0002) and (10$\bar{1}$0) pole figures, (e) Table summarizing the Euler angles of the corresponding parent and the predicted twin variants with their respective Schmid factor and color code for Fig. 11c, (f) Measured and predicted volume fraction of the parent grain and the twin variants. (For interpretation of the references to color in this figure legend, the reader is referred to the Web version of this article.)

for both the parent and twin variants are compared in Figs. 11f and 12f for both grains (Grains 3 and 4), and indicate reasonably good agreement.

The tables inserted in Figs. 9–12 present the Schmid factors for the twin systems in the initial state. As can be seen by comparing them with the volume fractions, there is a systematic correlation between them. The higher the Schmid factor, the higher is the twinning volume of that variant.

With progressive deformation, the lenticular morphology of the extension twin variants broadens by virtue of twin boundary migration. Such growth phenomena of extension twin variants continue until they consume the available matrix. It is important to note here that for simplification purpose the twin variants are referred to as T_{1a}, T_{1b}, T_{2a}, T_{2b}, T_{3a} and T_{3b}, based upon the twin plane and directions; where a and b represent the twin variants belonging to the same pair. Fig. 13a–d displays the prediction of the growth phenomena of twin variants for grains 1, 2, 3 and 4, respectively. In the case of grains 1 and 2, the gradual evolution of the T_{1a}, T_{1b}, T_{2a} and T_{2b} is observed to be consuming the parent grains up to 95%. Moreover, it can be emphasized here that, for Grain 1, the growth of T_{1a} and T_{1b} were higher, whereas in Grain 2, T_{2a} and T_{2b} evolved at a higher rate owing to their respective higher shear rate. Likewise, for grains 3 and 4, T_{1a} and T_{1b} predominantly develops with strain. Apparently, for all the four grains, no trace for the T_{3a} and T_{3b} variants were obtained for the entire deformation process.

4.8.2. Statistical analysis on the activity of extension twin variants on 45 grains

Our grain-by-grain analysis for the comparison of predicted and experimental twinning activity was extended to 45 grains, for all twinning variants; the results are presented in Figs. 14–15. The global average volume of the parent grains and the six extension twin variants are presented in Fig. 14a. The first column in Fig. 14a shows the total relative volume fraction of the parent grains and the following six columns represent the same for the twins. As can be seen, there was practically no volume for the twin variants T_{3a} and T_{3b}; the maximum number of operating twin variants were four in a grain. The predicted global volume fractions are in good agreement with the experimental ones, for all twin variants.

The results obtained for the total twin volume fractions of the individual grains are presented in Fig. 14b. The activities of the individual twin variants are compared in Fig. 15. In order to ease the comparison between the experimental and the corresponding simulated values, they are connected with a small blue segment for each grain. The lengths of these segments illustrate the degree of the agreement. As can be seen, for most of the grains, the deviations are relatively small. The standard deviations of the individual twin

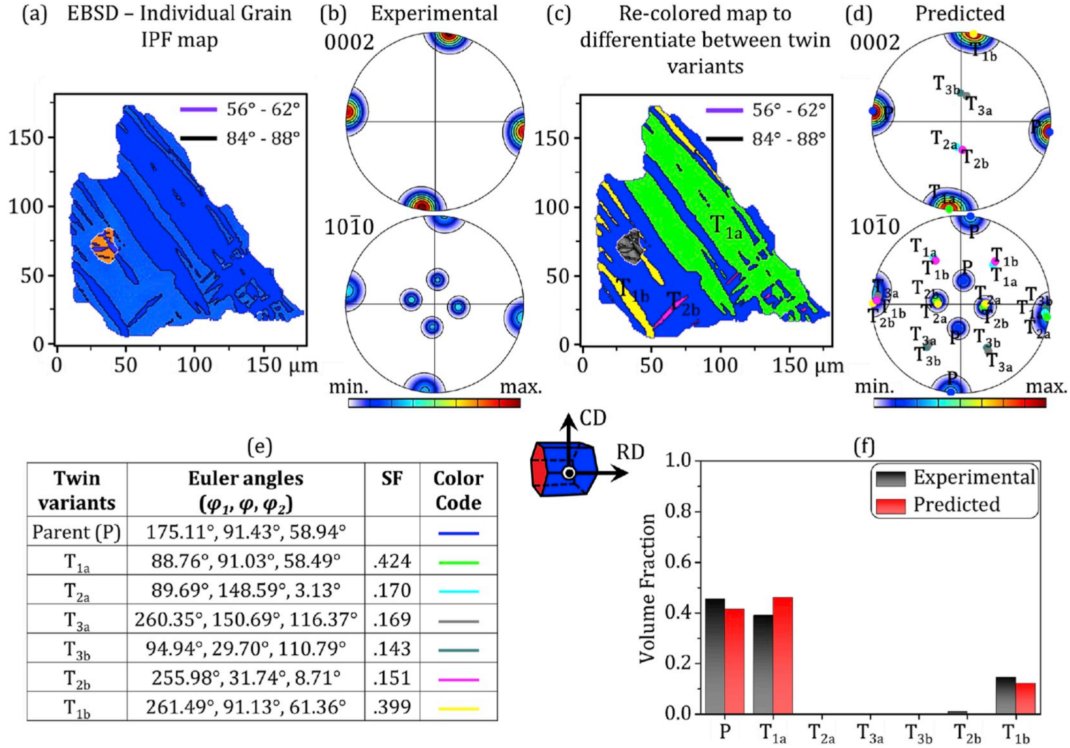

Twin variants	Euler angles ($\varphi_1, \varphi, \varphi_2$)	SF	Color Code
Parent (P)	175.11°, 91.43°, 58.94°		blue
T_{1a}	88.76°, 91.03°, 58.49°	.424	green
T_{2a}	89.69°, 148.59°, 3.13°	.170	cyan
T_{3a}	260.35°, 150.69°, 116.37°	.169	grey
T_{3b}	94.94°, 29.70°, 110.79°	.143	teal
T_{2b}	255.98°, 31.74°, 8.71°	.151	magenta
T_{1b}	261.49°, 91.13°, 61.36°	.399	yellow

Fig. 12. (a) Inverse pole figure map of Grain 4 with CD ‖ ~⟨10$\bar{1}$0⟩ (the parent orientation is represented by the HCP unit cell with reference directions, CD and RD), (b) its corresponding (0002) and (10$\bar{1}$0) pole figures, (c) Re-colored map showing twin variants in distinctive color plotted with respect to their predicted Euler angles, (d) Predicted (0002) and (10$\bar{1}$0) pole figures, (e) Table summarizing the Euler angles of the corresponding parent and the predicted twin variants with their respective Schmid factor and color code for Fig. 12c, (f) Measured and predicted volume fraction of the parent grain and the twin variants. (For interpretation of the references to color in this figure legend, the reader is referred to the Web version of this article.)

variants relative to the total experimental twin volumes in the grains are found to be as following: $T_{1a} = 5.14\%$, $T_{1b} = 3.43\%$, $T_{2a} = 4.95\%$, and $T_{2b} = 5.69\%$. As Fig. 15 shows, there was no significant twinning activity for the T_{3a} and T_{3b} variants. Note that, when the experimental value is practically identical with the predicted value for a few twin variants, one symbol (experimental) is hidden by the other.

5. Discussion

As shown in the preceding section, the present ATV approach embedded into the VPSC polycrystal model was able to reproduce several aspects of the extension twin induced deformation behaviour for compression testing of the Mg–3Al-0.3Mn alloy. They are the flow curve, deformation texture, and the volume fraction of extension twin variants, even locally on individual grains. Note that previous works on hexagonal materials were also successful for the flow curve and texture evolution, we cite as examples: Salem et al., (2003); Proust et al. (2007); Choi et al. (2010); Wang et al. (2010); Mu et al., (2014), but could not be applied locally, because the parent grain was replaced by one of its twin variants. All these previous simulations used the tangent approach within the VPSC model; the same was adopted in this work. Nevertheless, it is important to verify that the choice of the tangent model was the most precise approach, so further simulations were conducted by varying the value of the 'α' parameter in the interaction equation (Eq. (4)). This 'α' parameter influences the response of the grain critically with the surrounding equivalent medium for the polycrystal model. The results are discussed below.

5.1. Effect of the interaction parameter 'α'

A detailed description about the role of the 'α' parameter in VPSC modelling is described in previous studies (Mercier et al., 1995; Molinari and Toth, 1994a; Toth et al., 1997; Gu et al., 2013). In the present work, the value of the 'α' parameter was set equal to the strain rate sensitivity index: $\alpha = m$. This case is called the 'tangent approach' for material behaviour in VPSC modelling. We wanted to make sure that the tangent approach is the one which is applicable for every anisotropic crystal, in the present case, for hexagonal structures. Hence, simulations were also performed for other values of α and compared vis-à-vis with the experimental counterparts. Three simulations were carried out by varying the α parameter (all other parameters were kept constant); the values of $\alpha = 0.05$, 0.1,

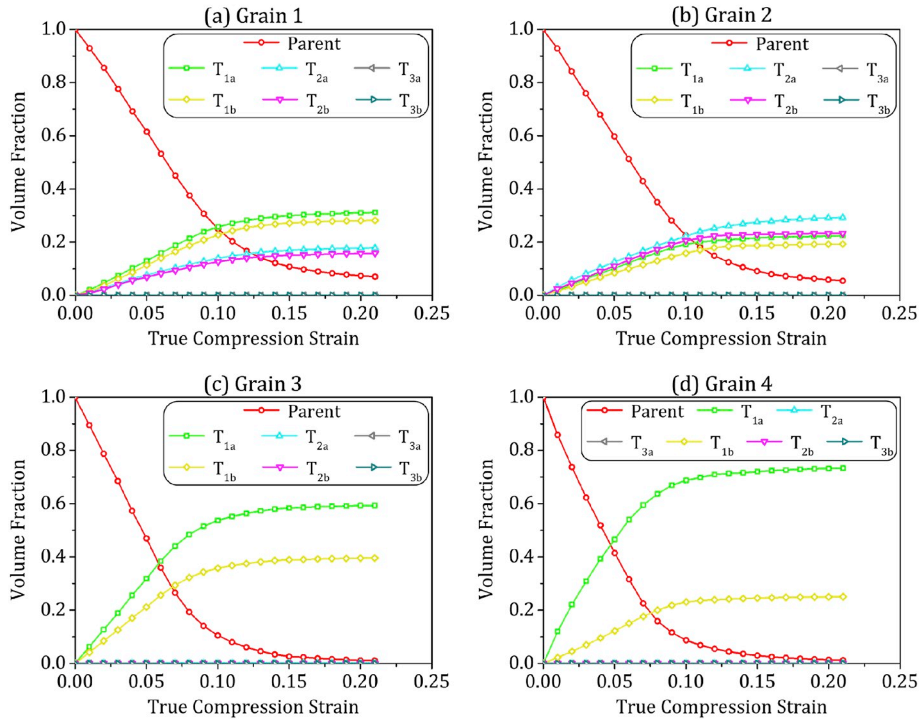

Fig. 13. Growth phenomena of twin variants as an implicit function of strain for: (a) Grain 1; (b) Grain 2; (c) Grain 3; (d) Grain 4.

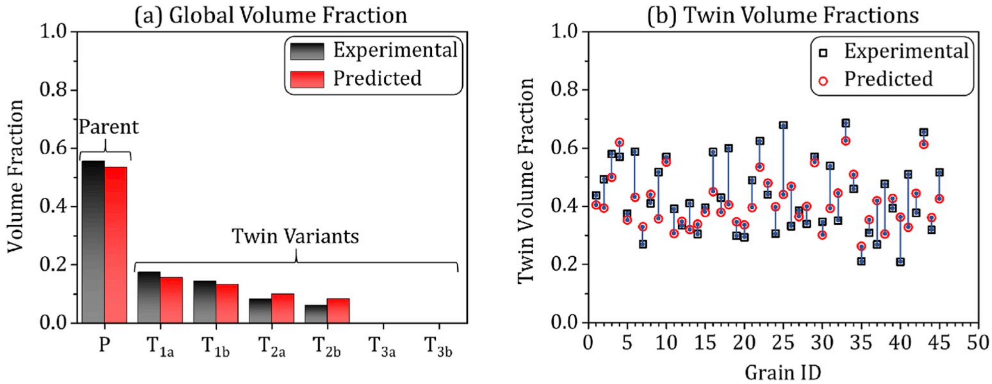

Fig. 14. Comparison of predicted and simulated twin volume fractions at 5% compression. (a): The global average volumes of the parent grains and the six twin variants obtained for 45 parent grains. (b): The total twin volumes for 45 individual grains.

0.3 and 0.5 were chosen. Fig. 16a–c presents the texture evolution in the form of (0002) and $(10\overline{1}0)$ pole figures for increasing strain for α = 0.05, 0.3 and 0.5. (Note that the case of α = 0.1, which was the adopted α value, is presented already in Fig. 3a.).

It can be seen in Fig. 16a that when $\alpha = 0.05$, the texture evolution occurred at a much faster rate and had a higher intensity as compared to the experimental observations. For $\alpha = 0.1$, the prediction of texture evolution (as shown in Fig. 3a) with strain was the most appropriate compared to the experiments. On the other hand, for $\alpha = 0.3$ and 0.5, the progress of the texture evolution and its intensity was much reduced (Fig. 16b and c) as compared to the experimental measurements for all strain values.

Fig. 17a shows the discrepancies in the predicted flow curves as the interaction parameter (α) is varied. It can be seen that the best agreement with the experimental sigmoidal flow curve was obtained for $\alpha = 0.1$. Simultaneously, the volume fraction of the twin is plotted for different α-values in Fig. 17b. For $\alpha = 0.05$, the predicted volume fraction of extension twins increases at a faster rate than the experimentally observed. As the α-value is increased, the evolution rate of the predicted extension twin volume fraction decreased with deformation. Again, a good correlation between the experiment and the simulation was obtained for $\alpha = 0.1$. The difference in the predicted twin volume fraction manifests that the rate of volume transfer from the parent to the twin orientations is strongly influenced by the α-value.

Moreover, it can be emphasized that the variation in the simulated texture (Fig. 16), strain hardening response (Fig. 17a) and twin-

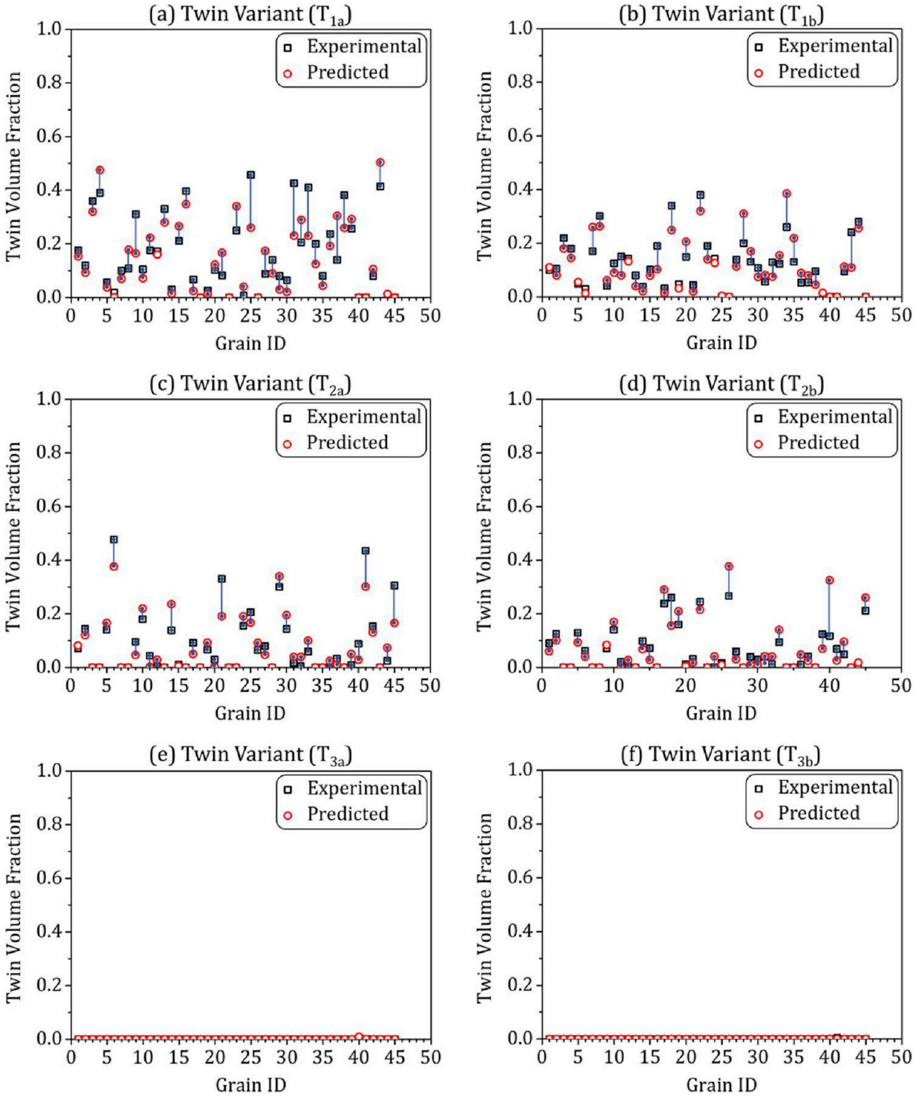

Fig. 15. Individual analysis of the activities of the six extension twin variants for 45 grains. The corresponding experimental and simulated values are connected with a small blue segment. (Note that when only the predicted symbol appears, it means the two values are coinciding.). (For interpretation of the references to color in this figure legend, the reader is referred to the Web version of this article.)

volume fraction evolution with the strain (Fig. 17b) could be related to the activities of the extension twins as well as dislocation slip. In this aspect, the activities of the deformation modes predicted by the ATV model with varying α parameter is shown in Fig. 18. For $\alpha = 0.05$, the extension twins were the most active initially, then gradually decreased (Fig. 18a). This can be related to the premature saturation of twinning (Fig. 17b). For $\alpha = 0.3$ and 0.5, the extension twin activities decreased and became progressively lower than the prismatic slip. At the same time, the variation in slip activities can also be seen with the change in the 'α' parameter. For instance, at lower strain regime ($\varepsilon < 0.10$), when $\alpha = 0.05$ (Fig. 18a), the deformation is mainly guided by the two most active slip systems (basal and prismatic, simultaneously), for the entire polycrystal. On the other hand, as the 'α' parameter is increased, the activity of the basal slip systems is gradually reduced, and the deformation is primarily governed by the most active prismatic slip systems. Due to such differences in the operating deformation modes at the lower strain regime, the strain hardening response was also varying, as shown in the inset of Fig. 17a.

Conversely, at higher strain regime ($\varepsilon > 0.10$), the activity plot (Fig. 18) portrays that the pyramidal $\langle c + a \rangle$ slip systems solely contributed to the plastic deformation for all 'α' values. A direct consequence is that the pyramidal $\langle c + a \rangle$/I mark the highest activity as compared to the pyramidal $\langle c + a \rangle$/II. However, with increasing 'α' value, the pyramidal $\langle c + a \rangle$/II activity slightly decreases, while the activity of pyramidal $\langle c + a \rangle$/I slip remained almost constant. Correspondingly, it affected the strain hardening response (Fig. 17a) which clearly depicts that for $\alpha = 0.05$, 0.1, and 0.3, the variation in the predicted strain hardening response is quite small; except for $\alpha = 0.5$, which shows moderate deviation.

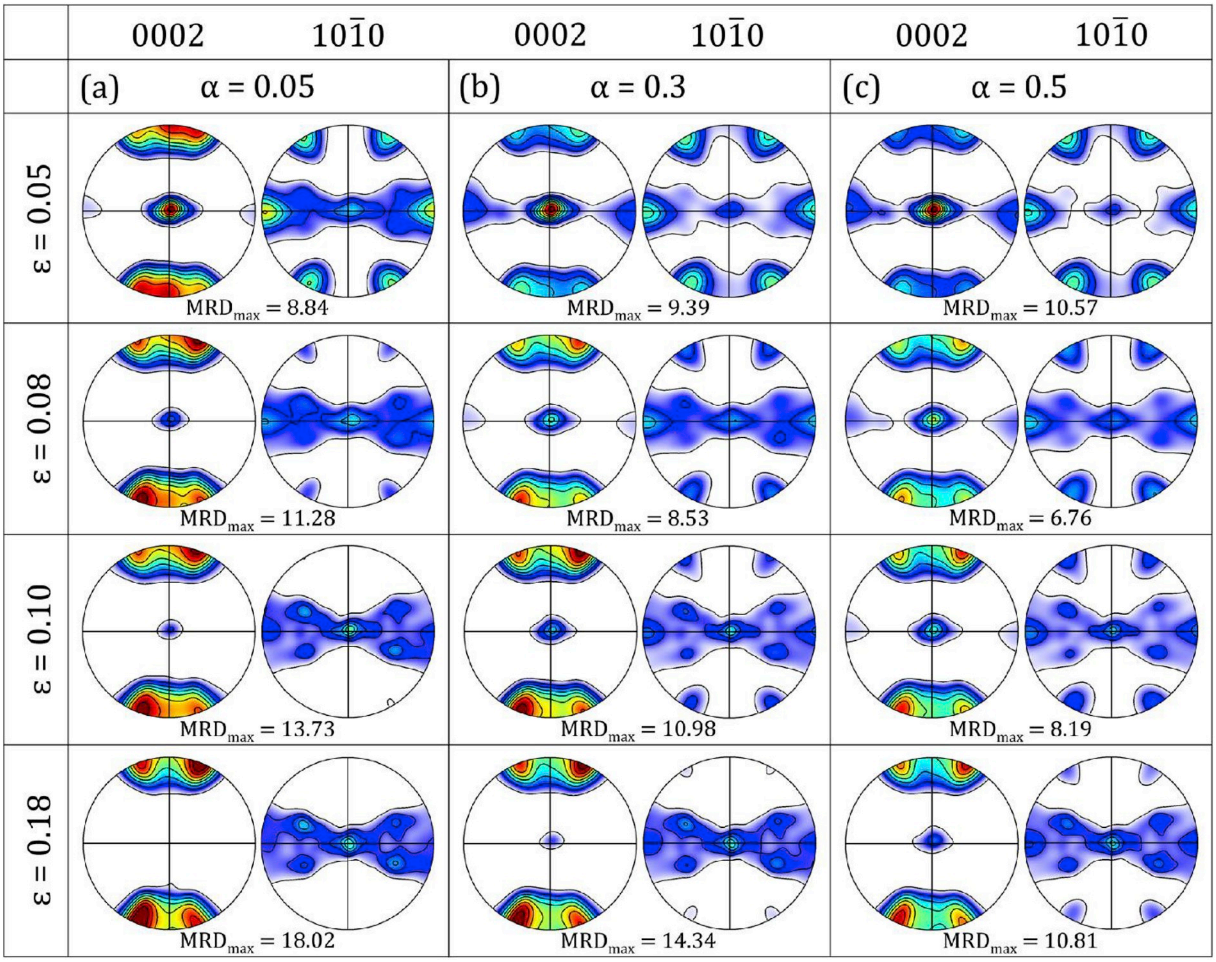

Fig. 16. Evolution of texture as an implicit function of interaction parameter, α = 0.05, 0.3, and 0.5. The intensity color scale is the same as illustrated in Fig. 3. (For interpretation of the references to color in this figure legend, the reader is referred to the Web version of this article.)

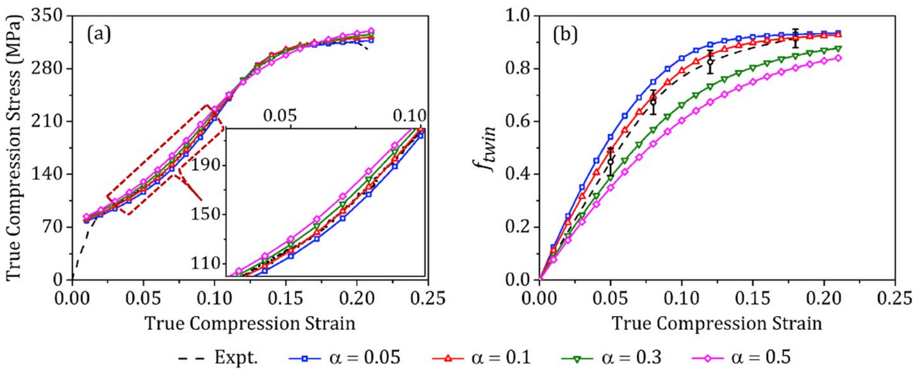

Fig. 17. Variation in the predicted (a) flow curve; and (b) extension twin volume fraction; as the implicit function of interaction parameter, α = 0.05, 0.1, 0.3 and 0.5. The black curve represents the experimental measurements.

5.2. Analysis of twin activity

Our simulation results presented in Fig. 14a shows good agreement for the average volume fractions of the twins and parent phases. The most active twin variants are the T_{1a} and T_{1b}, while T_{2a} and T_{2b} are about twice less active than T_{1a} and T_{1b}. It is to be noted that variants T_{3a} and T_{3b} were not activated in any of the 45 grains examined. The good average agreement proves that the presented ATV

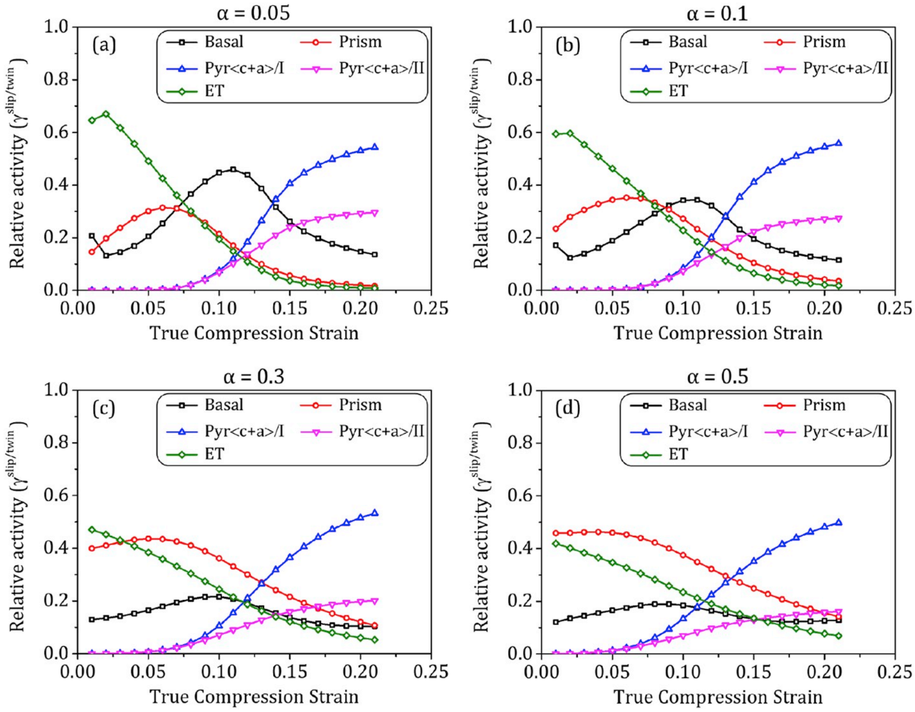

Fig. 18. Variations in the activities of various slip and extension twin deformation modes predicted by the ATV approach as a function of true compression strain for (a) α = 0.05; (b) α = 0.1; (c) α = 0.3; (d) α = 0.5.

approach implemented into the VPSC model can accurately predict the average twin activities.

The individual *grain-by-grain total twin volumes* displayed in Fig. 14b is also showing relatively good agreements between simulation and experiment. The deviations are illustrated by the lengths of the small blue segments in the figure that connect the corresponding experimental and simulated values. They are relatively significant for around 10 grains, being in the range of about 20–30%. Whilst for 35 grains, the deviations are less than 10%. One can attribute these deviations to be the effects of neighbouring grains. Indeed, the direct neighbourhood is not considered in the self-consistent model. In a similar analysis, carried out on twinning in TWIP steel using crystal plasticity finite element simulations, that is, considering topological effects - significant deviations were obtained for 55 grains as reported by Dancette et al. (2012). It is, however, expected that better agreement should be obtained when the topology is included in the simulation compared to a modelling where it is neglected, like in the present work.

As the applied ATV approach permits to follow the twin volume evolution for each variant, a grain-by-grain and variant-to-variant analysis are presented in Fig. 15 for 45 grains. As can be seen, the number of operating twinning systems goes up to four, with significant volumes in all variants for many grains. The deviation between experiment and simulation are of the same level as for the total volumes discussed in the previous paragraph. The agreement can be considered excellent, and it is the first time that a modelling is predicting the twinning activity up to the details, as shown in Fig. 15. The success of the simulation is, however, somewhat unexpected. As already discussed above, the present simulation is not considering the effects of the neighbours, while the effect of the neighbouring grain on the twinning activity is reported in several studies (Beyerlein et al., 2010a; Barnett et al., 2012; Khosravani et al., 2015; Kumar et al., 2019). This peculiarity of the present modelling needs a detailed discussion, which is developed below.

The triggering of twins in neighbouring parent grains due to the formation of twin lamellae on the other side of the grain boundary is a well-known phenomenon and can often lead to an avalanche kind of twinning across several grains upon continued straining (Barnett et al., 2012). Such evidence of twin transmission has been statistically studied by Beyerlein et al. (2010) and Khosravani et al. (2015). They demonstrated that the probability of twin transmission increases with the decrease in grain boundary misorientation. For instance, in the case of Mg alloys, twin transmission is significant for grain boundaries with misorientation less than 45° (Kumar et al., 2019). In our current study, traces of twin transmission could be well observed in the IPF map of the sample strained to a strain of 0.05 (see Fig. 4a, $\varepsilon = 0.05$). At the same time, our statistical investigation on individual grains coupled with the VPSC-ATV approach (Figs. 9–12, 14, 15) revealed that very successful prediction could be achieved without considering the neighbours. A possible explanation of this is that the key factor that determines the twinning activity is the *orientation* of the grain, not the neighbourhood. The neighbours can play a role in the nucleation mechanism of the twins; however, the growth phenomenon is mainly controlled by the orientation of the parent grain. It can be seen when comparing experiment and simulation for cases when twin transmission is happening that the VPSC-ATV model predicts the high activity of both twins that are participants of the transmission. Such cases are present in Fig. 4a and also in previous VPSC-ATV work (Gu et al., 2014), applied for low cycle fatigue of AZ31, where even for avalanche type of twinning, the simulation is correctly predicting the twins that form along the path of the avalanche (see in Fig. 2 of

Gu et al., 2014). Therefore, the effect of neighbour grain is restricted to determine the twin nucleation sites at the grain boundary. After nucleation, the growth is not controlled by the neighbouring grain; rather, it is governed by the orientation of the grain and hence can be correctly predicted by the VPSC-ATV approach. It can be concluded that transmission or avalanche types of twins only appear interconnected because of their nucleation process and the effect of neighbours is only for this. This is why, even by neglecting the neighbours, the VPSC-ATV approach is successful. The essential in modelling of twinning is that the modelling approach has to be well developed, which is the case when all twin variants are correctly accounted for and considered as grains with their corresponding forms, as presented in this VPSC-ATV approach.

5.3. *Understanding the strain hardening response*

The accurate simulation of the three strain hardening stages can only be obtained if the estimation of the CRSS for dislocation slip and twinning along with the hardening parameters of the respective parent and twin orientations are precise. Previous studies on Mg and its alloys had also revealed similar strain hardening behaviour when the extension twinning was the favourable mechanism (Knezevic et al., 2010; Mu et al., 2011, 2014; Guo et al., 2015). It is well ascertained that during deformation, nucleation of twin events is typically followed by the propagation and growth phenomena till it reaches the edge of the parent grain. These findings substantiate our present experimental investigation while also supporting the presented ATV approach.

5.3.1. *Stage I hardening*

Stage I (from $\varepsilon = 0.015$ to 0.03) is characterized by a rapid drop in SHR (Fig. 2b), which is arising due to elastic-plastic transition during the early stage of deformation leading to micro-yielding. The ATV model could not capture this stage appropriately. However, it is well known from the literature that early activation of primary slip systems, most probably the basal (Mu et al., 2011, 2014; Guo et al., 2015) or prismatic slip (Agnew et al., 2003, 2005; Keshavarz and Barnett, 2006; Ulacia et al., 2010) can lower the SHR. In our calculation, the initial strength for the basal slip was considered the lowest, 27 MPa, followed by the strength for the prismatic slip, with 52 MPa. However, for the present deformation configuration of the initial material, the Schmid factor for basal slip was found out to be nearly ~0.00, since the basal planes of TD orientations were parallel to the CD, while for prismatic slip, the SF was ~0.49. Therefore, the lowering of the SHR can be related to prismatic $\langle a \rangle$ slips.

5.3.2. *Stage II hardening*

Stage II (from $\varepsilon = 0.03$ to 0.10) and stage III (beyond $\varepsilon = 0.10$) could be accurately captured by the ATV approach. In fact, Stage II is characterized by an increase in the hardening rate (Fig. 2b). This is primarily attributed to the increase and dominance of deformation-induced extension twinning activities over the dislocation slip (Fig. 6c). From the microstructural point of view, various extension twin variants evolve and grow within the parent grains with increasing strain. At $\varepsilon \approx 0.05$, the nucleation and growth of extension twins lead to a decrease in the average grain size. However, as deformation progressed, the broadening of the extension twins occurred gradually consuming the parent matrix, thereby increasing the average grain size. A detailed investigation performed by Sahoo et al. (2019) indicates that the Hall-Petch effect is not responsible for the sigmoidal strain-hardening behaviour.

Concerning crystallographic orientation, extension twins abruptly reorient the initial orientation by ~86.4° about the $\langle 11\bar{2}0 \rangle$ axes. This leads to the formation of near $\langle 0002 \rangle||$CD texture components. Previous TEM studies (Morozumi et al., 1976; Agnew et al., 2002; Dixit et al., 2015; Wang and Agnew, 2016) observed the presence of both $\langle c + a \rangle$ and $\langle a \rangle$ dislocations during twin-induced deformation of Mg alloy. Indeed, the activity of $\langle c + a \rangle$ slip systems within the twin domain have been frequently reported and are considered as hard glide systems (Knezevic et al., 2010; Dixit et al., 2015). As a result, it can be pointed out that the increase in the $\langle c + a \rangle$ dislocation activities can lead to high strain hardening. Furthermore, it can also be emphasized that the (0002) texture components parallel to the compression axis are texturally harder and therefore impart higher resistance to deformation compared to the initially present prismatic type texture. In contrast, Basinski type hardening does not exist in this case as the twin boundary movements do not get restricted with increasing deformation (Knezevic et al., 2010; Oppedal et al., 2012; Dixit et al., 2015). Knezevic et al. (2010) have shown that extension twins in polycrystalline Mg alloys appear at very low strains when macroscopic stress is also low and are known to grow rapidly. Oppedal et al. (2012) have shown that the higher hardening in the twins over parent matrix may not be related to the increase in the dislocation generation due to the Basinski effect. Rather, it could be due to latent hardening resulting from the increased dislocation multiplication within the twin domains. On continued deformation, the volume fraction of these texturally hard extension twin domains increases, and a sigmoidal shaped flow curve often appears (Fig. 2a), followed by an increase in the SHR (Fig. 2b).

The predicted slip and twin activity plot in Fig. 6c indicates that the prismatic slip systems remain more active as compared to basal slip in most part of Stage II. This is due to the higher shear rate associated with the prismatic slip compared to basal for the parent orientations with respect to the loading condition. The high activity of prismatic slip is more prominent for the parent matrix and can be seen in Fig. 6a. This occurred even though the slip resistance for prismatic slip was much higher than for basal slip. It can be suggested that once the twin activity decreases, the majority of the strain is accommodated by the prismatic slip in the parent matrix (Fig. 6a) and by the growth of the twin variants. The prominent role of prismatic slip during deformation of Mg alloys have been reported by several authors (Koike et al., 2003; Armstrong and Walley, 2008; Ulacia et al., 2010). They emphasized its existence mostly near grain boundaries, in order to maintain grain boundary contiguity. Studies on in-plane tension and compression by in-situ neutron diffraction have also revealed that the macroscopic yielding is closely associated with the activation of prismatic slip (Agnew et al., 2003).

5.3.3. Stage III hardening

Stage III shows a continuous decrease in SHR with the strain (Fig. 2b). The beginning of this stage is marked as peak strain ($\varepsilon_p = \sim 0.10$) and denotes the saturation of deformation-induced extension twin growth. Microstructural observation at this strain ($\varepsilon = \sim 0.10$) also signifies the same (Fig. 4a, $\varepsilon = \sim 0.10$). This implies a significant reduction in the number of available potent sites in the parent-matrix for further nucleation and growth of extension twins. The prior prismatic slip in the parent matrix leads to the progressive orientation of basal poles at $\sim 45°$ to CD (Fig. 3b). This leads to an increase in the activities of the basal slip in this region. In the same instance, the twin domains can either deform by dislocation slip or by contraction twins (Knezevic et al., 2010; Khan and Yu, 2012; Dixit et al., 2015; Chouhan et al., 2019). The present investigation (Fig. 6b) shows that the activities of basal slip decreases and significant activities of pyramidal $\langle c+a \rangle$/I and II type dislocation slip take place inside the twin domains. From this strain ($\varepsilon_p = \sim 0.10$) onwards, the twin domains have their crystallographic c-axis almost parallel to the imposed compression direction. This configuration is the most preferable for the activation of pyramidal $\langle c+a \rangle$/I and II type dislocation slip. The activity plots (Fig. 6b and c) also indicate the same with the highest activity for pyramidal $\langle c+a \rangle$/I type dislocations and less contribution from pyramidal $\langle c+a \rangle$/II. This finding corroborates well with recent experimental (Xie et al., 2016) and computational observations performed on c-axis compression of Mg single crystals (Fan et al., 2017, 2017; Srivastava and El-Awady, 2017).

Additionally, the activity plot for the twin domains (Fig. 6b) shows no trace of prismatic slip and displays a gradual reduction in the basal dislocation slip activities. Knezevic et al. (2010) and Dixit et al. (2015) suggested that during compression of Mg alloys, the twin domain produces plastic deformation via $\langle c+a \rangle$ slip and contraction twinning. In the present work, no contraction twins were detected up to fracture strain. Therefore, it can be emphasized that the stress concentration associated during compression along the c-axis might not have reached the threshold value to initiate contraction twins. Hence, the present investigation reveals that the pyramidal $\langle c+a \rangle$type dislocation slip occurred within the twin domain leading to slip-based deformation and a decrease in SHR. Accordingly, it is important to emphasize that prismatic slip activity is dominant when the twin volume fraction is low, marked as Stage II ($\varepsilon = \sim 0.03$ - ~ 0.10). Eventually, prismatic slip drops in favour of pyramidal $\langle c+a \rangle$ slip within the twin domains, marked as Stage III ($\varepsilon = \sim 0.10$ - ~ 0.20).

5.4. Hardening of twins

The present ATV approach considers a higher hardening coefficient for the extension twin domains (1350 MPa) as compared to the parent matrix phase (67 MPa), allowing it to behave as a composite (Agnew et al., 2003; Sahoo et al., 2019). Besides, the hardening approach, as described in Section 2, considers the effect of both self and latent hardening for the parent and twin phases. These two combined effects led to a precise prediction of the flow curve. It is worth mentioning that the hardening in the parent domain does not contribute towards sigmoidal shape strain hardening because the volume fraction of the matrix is decreasing. Thus, the major contribution comes from the twin domains, which gradually evolve during deformation with increasing volume. As a consequence, the effect of self and latent hardening in the twin domains is enhanced due to the activation of pyramidal $\langle c+a \rangle$/I and $\langle c+a \rangle$/II slip systems, which require much higher stress. Henceforth, it is reasonable to state that the hardening is caused by the abrupt crystallographic reorientation of the c-axis towards the compression direction (referred to as geometrical hardening), and due to the higher self and latent hardening within the twin domain. The former effect was considered in the present approach by assigning a higher

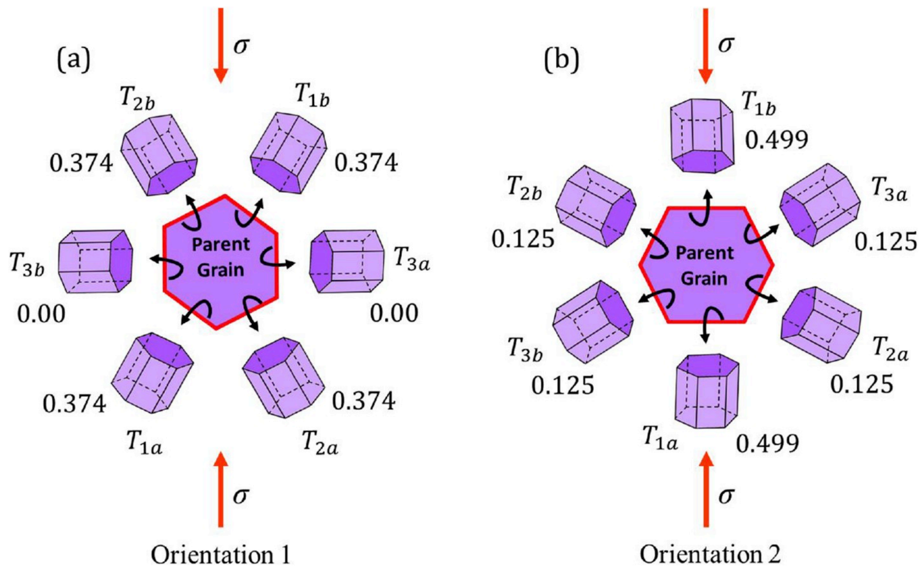

Fig. 19. Crystallographic geometry of the extension twin variants for the parent orientations: (a) CD$\|\langle 11\bar{2}0 \rangle$ and (b) CD$\|\langle 10\bar{1}0 \rangle$ and their corresponding Schmid factors for these ideal configurations.

hardening coefficient for the twin domain compared to the parent matrix. While the latter effect is accounted for by the pyramidal $\langle c + a \rangle$ slip system activities.

5.5. Deformation induced twin variant selection

In this section, the kinetics of the preferential evolution of specific twin variants for compression along $\langle 11\bar{2}0 \rangle - \langle 10\bar{1}0 \rangle$ fibre axis is addressed. Fig. 19a and b demonstrate the ideal positions of the twin variant pairs (T_{1a}, T_{1b}, T_{2a}, T_{2b}, T_{3a} and T_{3b}) with respect to the parent orientations possessing $\langle 11\bar{2}0 \rangle||$CD and $\langle 10\bar{1}0 \rangle||$CD fibre type textures, analogous to Grain 1, 2 (Figs. 9 and 10), and Grain 3, 4 (Figs. 11 and 12), respectively. These extreme geometrical configurations are associated with 30° rotation about the [0002] axis. Consequently, the activation of twin variants can be readily marked by the spread in these extension twin texture components from one extreme position (Fig. 19a) to another (Fig. 19b). The Schmid factor for the respective extension twin variants is also included in Fig. 19a and b. It is to be noted here that; the variant pairs possess similar Schmid factors. In general, this holds true for the ideal orientation, where the c-axis is exactly normal to the compression direction. However, under realistic conditions, the c-axis may deviate; consequently, the Schmid factor for the variant-pair may also vary, thereby affecting their evolution rate. Although the VPSC model uses shear-rate based calculation for determining the activity of the twin variants, the Schmid factor can also be used to understand the preferential activity of the extension twin variants during the deformation as exemplified in previous works (Park et al., 2010; Mu et al., 2011; El Kadiri et al., 2013b; Xin et al., 2016).

The strain path dependence of extension twinning in polycrystalline Mg alloys has been demonstrated by several authors (Nave and Barnett, 2004; Jiang et al., 2007a; El Kadiri et al., 2013b; Mu et al., 2014; Mokdad et al., 2017) relating the existence of parallel and/or crossing type twin morphology. However, the factors governing such morphological features still require focus. Thus for the configuration in Fig. 19a, where the compression direction is along the $\langle 11\bar{2}0 \rangle$ axis, the evolution of 'T_{1a} and T_{1b}' as well as 'T_{2a} and T_{2b}' are equally feasible (owing to their high SF $\approx$ 0.374), 'T_{3a} and T_{3b}' will not form as their SF is zero. This leads to the evolution of cross twin type lenticular morphology. However, for the situation in Fig. 19b with $\langle 10\bar{1}0 \rangle||$CD, '$T_{1a}$ and T_{1b}' will predominantly form (as the SF $\approx$ 0.499), whereas the evolution of 'T_{2a}, T_{2b}' and T_{3a}, T_{3b}' would be negligible (SF $\approx$ 0.125). The evolution of only a single extension twin pair results in the formation of lamellar and almost parallel-twin morphology.

In this paper, we dealt with experiments and simulations only for loading direction parallel to the bar extrusion axis. We repeated the same experimental and modelling analysis for another loading direction: perpendicular to the extrusion axis. In order to save space, we do not present here those results, only confirm that the same principles were found as for the presented loading direction.

6. Summary and conclusions

The all twin variant (ATV) approach for the polycrystal simulation was employed in this work to model the extension twins induced: (i) strain hardening response, (ii) evolution of twin volume fraction, and (iii) texture evolution for the polycrystalline Mg–3Al-0.3Mn alloy. The model does not impose any variant selection criteria; rather, the evolution of twins was naturally computed as a function of their pseudo-shear-rate. The growth of the twin variants was computed by the gradual transfer of volume from the parent matrix into the twin variants. A reasonable quantitative agreement between the computed and experimental counterparts was obtained. In order to examine the appropriateness of the proposed model, individual grain analysis was also accomplished. A good correlation was obtained for the volume fractions of the computed and experimental extension twin variants. The characteristic ingredients of the present model are highlighted in the following conclusions:

i. The twin induced deformation behaviour leading to a sigmoidal shaped flow curve could be appropriately reproduced by employing the ATV approach embedded into the VPSC model. A higher hardening coefficient for the extension twins with respect to the parent matrix is required to reproduce the experimental stress-strain curve. Textural hardening due to lattice reorientation and intrinsic latent hardening due to multiple pyramidal $\langle c + a \rangle$/I and $\langle c + a \rangle$/II slip systems are important elements of strain hardening, which were taken into account through the hardening law.
ii. The ATV model does not only predict the predominant twin variants but appropriately computes the evolution of all twin variants' volume fraction. The good agreement between computed and experimentally obtained twinning activity in individual grains validates the presented approach.
iii. The model indicates that even though the strength for basal slip is lower than for prismatic slip, the latter was more active in the parent matrix phase. Upon progressive deformation, the extension twin domains gradually encompassed the microstructure. The deformation in the twin domain was initially accommodated via basal slip and later by the activation of pyramidal $\langle c + a \rangle$/ I and $\langle c + a \rangle$/II type slip system.
iv. The model deciphers the mechanism behind the evolution of extension twin variants as a function of grain orientation relative to the loading direction. Compression along $\langle 11\bar{2}0 \rangle||$CD results in the evolution of two pairs of extension twin variant, namely 'T_{1a}, T_{1b}' and 'T_{2a}, T_{2b}' leading to intersecting lenticular morphology. Whereas, compression along $\langle 10\bar{1}0 \rangle||$CD leads to the evolution of predominant 'T_{1a}, T_{1b}' pair thereby forming parallel lamellar morphology. Nevertheless, for both cases, the third variant pair, i.e., 'T_{3a}, T_{3b}' always remained inactive.
v. The excellent agreement between simulation and experiment obtained by the VPSC - ATV model for the activities of the twin variants of individual grains indicate that the major factor for predicting twinning activity is the crystallographic orientation of the parent grain. Neighbours affect the nucleation only, so they remain secondary with respect to the crystal orientation.

It is worth mentioning that the ATV model can be extended to other polycrystalline materials where both slip and twin contributes to plastic deformation.

CRediT authorship contribution statement

Sudeep K. Sahoo: Software, Validation, Formal analysis, Investigation, Data curation, Writing - original draft, Writing - review & editing, Visualization. **Somjeet Biswas:** Conceptualization, Methodology, Validation, Formal analysis, Resources, Writing - original draft, Writing - review & editing, Visualization, Supervision, Project administration, Funding acquisition. **Laszlo S. Toth:** Software, Validation, Formal analysis, Resources, Data curation, Writing - review & editing, Visualization, Supervision. **P.C. Gautam:** Investigation. **Benoît Beausir:** Software.

Acknowledgments

The authors acknowledge the financial support provided by the Science and Engineering Research Board (Ref. no.: ECR/2016/000125), Department of Science and Technology, Government of India. The work was also supported by the National Research Agency, France referenced as ANR-11-LABX-008-01 (LabEx DAMAS). The work used the facility 'Light Metals and Alloys Research Lab' setup at the Department of Metallurgical and Materials Engineering, and Central Research Facility, both in Indian Institute of Technology, Kharagpur, India.

Appendix A. Supplementary data

Supplementary data to this article can be found online at https://doi.org/10.1016/j.ijplas.2020.102660.

References

Agnew, S.R., Duygulu, Ö., 2005. Plastic anisotropy and the role of non-basal slip in magnesium alloy AZ31B. Int. J. Plast. 21, 1161–1193.
Agnew, S.R., Horton, J.A., Yoo, M.H., 2002. Transmission electron microscopy investigation of ⟨c+a⟩ dislocations in Mg and α-solid solution Mg-Li alloys. Metall. Mater. Trans. A 33, 851–858.
Agnew, S.R., Mehrotra, P., Lillo, T.M., Stoica, G.M., Liaw, P.K., 2005. Crystallographic texture evolution of three wrought magnesium alloys during equal channel angular extrusion. Mater. Sci. Eng. A 408, 72–78.
Agnew, S.R., Tomé, C.N., Brown, D.W., Holden, T.M., Vogel, S.C., 2003. Study of slip mechanisms in a magnesium alloy by neutron diffraction and modeling. Scr. Mater. 48, 1003–1008.
Agnew, S.R., Yoo, M.H., Tomé, C.N., 2001. Application of texture simulation to understanding mechanical behavior of Mg and solid solution alloys containing Li or Y. Acta Mater. 49, 4277–4289.
Allen, R.M., Toth, L.S., Oppedal, A.L., El Kadiri, H., 2018. Crystal plasticity modeling of anisotropic hardening and texture due to dislocation transmutation in twinning. Materials 11, 1855.
Al-Samman, T., Molodov, K.D., Molodov, D.A., Gottstein, G., Suwas, S., 2012. Softening and dynamic recrystallization in magnesium single crystals during c-axis compression. Acta Mater. 60, 537–545.
Ando, D., Koike, J., Sutou, Y., 2014. The role of deformation twinning in the fracture behaviour and mechanism of basal textured magnesium alloys. Mater. Sci. Eng. A 600, 145–152.
Ardeljan, M., Beyerlein, I.J., McWilliams, B.A., Knezevic, M., 2016. Strain rate and temperature sensitive multi-level crystal plasticity model for large plastic deformation behavior: application to AZ31 magnesium alloy. Int. J. Plast. 83, 90–109.
Armstrong, R.W., Walley, S.M., 2008. High strain rate properties of metals and alloys. Int. Mater. Rev. 53, 105–128.
ASTM E9-09, 2018. Standard Test Methods of Compression Testing of Metallic Materials at Room Temperature. ASTM International, West Conshohocken, PA. www.astm.org.
Barnett, M.R., 2007. Twinning and the ductility of magnesium alloys. Mater. Sci. Eng. A 464, 1–7.
Barnett, M.R., Keshavarz, Z., Beer, A.G., Atwell, D., 2004. Influence of grain size on the compressive deformation of wrought Mg–3Al–1Zn. Acta Mater. 52, 5093–5103.
Barnett, M.R., Nave, M.D., Ghaderi, A., 2012. Yield point elongation due to twinning in a magnesium alloy. Acta Mater. 60, 1433–1443.
Barrett, C.S., Haller, C.T., 1947. Twinning in polycrystalline magnesium. Trans. Am. Inst. Min. Metall. Eng. 171, 246–255.
Basinski, Z.S., Szczerba, M.S., Niewczas, M., Embury, J.D., Basinski, S.J., 1997. The transformation of slip dislocations during twinning of copper-aluminum alloy crystals. Rev. Métall. 94, 1037–1044.
Beausir, B., Fundenberger, J.J., 2017. Analysis Tools for Electron and X-Ray Diffraction, ATEX - Software. Université de Lorraine - Metz. www.atex-software.eu.
Beausir, B., Suwas, S., Toth, L.S., Neale, K.W., Fundenberger, J.-J., 2008. Analysis of texture evolution in magnesium during equal channel angular extrusion. Acta Mater. 56, 200–214.
Beyerlein, I.J., Capolungo, L., Marshall, P.E., McCabe, R.J., Tomé, C.N., 2010. Statistical analyses of deformation twinning in magnesium. Philos. Mag. 90, 2161–2190.
Beyerlein, I.J., McCabe, R.J., Tomé, C.N., 2011. Effect of microstructure on the nucleation of deformation twins in polycrystalline high-purity magnesium: a multi-scale modeling study. J. Mech. Phys. Solids 59, 988–1003.
Beyerlein, I.J., Tomé, C.N., 2010. A probabilistic twin nucleation model for HCP polycrystalline metals. Proc. Roy. Soc. A. 466, 2517–2544.
Biswas, S., Beausir, B., Toth, L.S., Suwas, S., 2013. Evolution of texture and microstructure during hot torsion of a magnesium alloy. Acta Mater. 61, 5263–5277.
Biswas, S., Brokmeier, H.-G., Fundenberger, J.-J., Suwas, S., 2015b. Role of deformation temperature on the evolution and heterogeneity of texture during equal channel angular pressing of magnesium. Mater. Char. 102, 98–102.
Biswas, S., Sahoo, S.K., Chouhan, D.K., Gautam, P.C., Shukla, A.J., 2018. Microstructure, texture evolution and dynamic recrystallization in Magnesium. Ref. Mod. MSME. https://doi.org/10.1016/B978-0-12-803581-8.10389-3.
Biswas, S., Singh, D.S., Beausir, B., Toth, L.S., Suwas, S., 2015a. Thermal response on the microstructure and texture of ECAP and cold-rolled Pure Magnesium. Metall. Mater. Trans. A 46, 2598–2613.
Biswas, S., Singh Dhinwal, S., Suwas, S., 2010. Room-temperature equal channel angular extrusion of pure magnesium. Acta Mater. 58, 3247–3261.
Bozzolo, N., Chan, L., Rollett, A.D., 2010. Misorientations induced by deformation twinning in titanium. J. Appl. Crystallogr. 43, 596–602.

Cheng, J., Ghosh, S., 2015. A crystal plasticity FE model for deformation with twin nucleation in magnesium alloys. Int. J. Plast. 67, 148–170.
Choi, S.-H., Kim, D.H., Park, S.S., You, B.S., 2010. Simulation of stress concentration in Mg alloys using the crystal plasticity finite element method. Acta Mater. 58, 320–329.
Chouhan, D.K., Singh, A.K., Biswas, S., Mondal, C., 2019. On the Strain-Hardening behavior and twin-induced grain refinement of CP-Ti under ambient temperature compression. Metall. Mater. Trans. A 1–20.
Christian, J.W., Mahajan, S., 1995. Deformation twinning. Prog. Mater. Sci. 39, 1-157.
Dancette, S., Delannay, L., Renard, K., Melchior, M.A., Jacques, P.J., 2012. Crystal plasticity modeling of texture development and hardening in TWIP steels. Acta Mater. 60, 2135–2145.
Dixit, N., Xie, K.Y., Hemker, K.J., Ramesh, K.T., 2015. Microstructural evolution of pure magnesium under high strain rate loading. Acta Mater. 87, 56–67.
Dudamell, N.V., Ulacia, I., Gálvez, F., Yi, S., Bohlen, J., Letzig, D., Hurtado, I., Pérez-Prado, M.T., 2011. Twinning and grain subdivision during dynamic deformation of a Mg AZ31 sheet alloy at room temperature. Acta Mater. 59, 6949–6962.
Eisenlohr, P., Diehl, M., Lebensohn, R.A., Roters, F., 2013. A spectral method solution to crystal elasto-viscoplasticity at finite strains. Int. J. Plast. 46, 37–53.
El Kadiri, H., Baird, J.C., Kapil, J., Oppedal, A.L., Cherkaoui, M., Vogel, S.C., 2013a. Flow asymmetry and nucleation stresses of {1012}twinning and non-basal slip in magnesium. Int. J. Plast. 44, 111–120.
El Kadiri, H., Barrett, C.D., Wang, J., Tomé, C.N., 2015. Why are {1012}twins profuse in magnesium? Acta Mater. 28, 354–361.
El Kadiri, H., Kapil, J., Oppedal, A.L., Hector, L.G., Agnew, S.R., Cherkaoui, M., Vogel, S.C., 2013b. The effect of twin–twin interactions on the nucleation and propagation of {1012}twinning in magnesium. Acta Mater. 61, 3549–3563.
El Kadiri, H., Oppedal, A.L., 2010. A crystal plasticity theory for latent hardening by glide twinning through dislocation transmutation and twin accommodation effects. J. Mech. Phys. Solids 58, 613–624.
Fan, H., El-Awady, J.A., 2015. Towards resolving the anonymity of pyramidal slip in magnesium. Mater. Sci. Eng. A 644, 318–324.
Fan, H., Wang, Q., Tian, X., El-Awady, J.A., 2017. Temperature effects on the mobility of pyramidal $\langle c+a \rangle$dislocations in magnesium. Scr. Mater. 127, 68–71.
Fernández, A., Pérez Prado, M.T., Wei, Y., Jérusalem, A., 2011. Continuum modeling of the response of a Mg alloy AZ31 rolled sheet during uniaxial deformation. Int. J. Plast. 27, 1739–1757.
Friák, M., Hickel, T., Grabowski, B., Lymperakis, L., Udyansky, A., Dick, A., Ma, D., Roters, F., Zhu, L.-F., Schlieter, A., Kühn, U., Ebrahimi, Z., Lebensohn, R.A., Holec, D., Eckert, J., Emmerich, H., Raabe, D., Neugebauer, J., 2011. Methodological challenges in combining quantum-mechanical and continuum approaches for materials science applications. Eur. Phys. J. Plus 126, 1–22.
Ghaderi, A., Barnett, M.R., 2011. Sensitivity of deformation twinning to grain size in titanium and magnesium. Acta Mater. 59, 7824–7839.
Graff, S., Brocks, W., Steglich, D., 2007. Yielding of magnesium: from single crystal to polycrystalline aggregates. Int. J. Plast. 23, 1957–1978.
Gu, C.F., Toth, L.S., 2012. Polycrystal modeling of tensile twinning in a Mg alloy during cyclic loading. Scr. Mater. 67, 673–676.
Gu, C.F., Toth, L.S., Field, D.P., Fundenberger, J.J., Zhang, Y.D., 2013. Room temperature equal-channel angular pressing of a magnesium alloy. Acta Mater. 61, 3027–3036.
Gu, C.F., Toth, L.S., Hoffman, M., 2014. Twinning effects in a polycrystalline magnesium alloy under cyclic deformation. Acta Mater. 62, 212–224.
Guo, X.Q., Chapuis, A., Wu, P.D., Agnew, S.R., 2015. On twinning and anisotropy in rolled Mg alloy AZ31 under uniaxial compression. Int. J. Solids Struct. 64–65, 42–50.
Gurao, N.P., Suwas, S., 2014. Generalized scaling of misorientation angle distributions at meso-scale in deformed materials. Sci. Rep. 4, 1–6.
Hazeli, K., Kannan, V., Kingstedt, O., Ravichandran, G., Ramesh, K., 2018. Deformation Twin Nucleation and Twin Variant Selection in Single Crystal Magnesium as a Function of Strain Rate arXiv preprint arXiv:1801.10252.
Homayonifar, M., Mosler, J., 2011. On the coupling of plastic slip and deformation-induced twinning in magnesium: a variationally consistent approach based on energy minimization. Int. J. Plast. 27, 983–1003.
Homayonifar, M., Mosler, J., 2012. Efficient modeling of microstructure evolution in magnesium by energy minimization. Int. J. Plast. 28, 1–20.
Hu, Y., Randle, V., 2007. An electron backscatter diffraction analysis of misorientation distributions in titanium alloys. Scr. Mater. 56, 1051–1054.
Hutchinson, J.W., 1976. Bounds and self-consistent estimates for creep of polycrystalline materials. Proc. Roy. Soc. A. 348, 101–127.
Jahedi, M., McWilliams, B.A., Moy, P., Knezevic, M., 2017. Deformation twinning in rolled WE43-T5 rare earth magnesium alloy: influence on strain hardening and texture evolution. Acta Mater. 131, 221–232.
Jain, A., Agnew, S.R., 2007. Modeling the temperature dependent effect of twinning on the behaviour of magnesium alloy AZ31B sheet. Mater. Sci. Eng. A 462, 29–36.
Jain, A., Duygulu, O., Brown, D.W., Tomé, C.N., Agnew, S.R., 2008. Grain size effects on the tensile properties and deformation mechanisms of a magnesium alloy, AZ31B, sheet. Mater. Sci. Eng. A 486, 545–555.
Jiang, J., Godfrey, A., Liu, W., Liu, Q., 2008. Identification and analysis of twinning variants during compression of a Mg–Al–Zn alloy. Scr. Mater. 58, 122–125.
Jiang, L., Jonas, J.J., Mishra, R.K., Luo, A.A., Sachdev, A.K., Godet, S., 2007a. Twinning and texture development in two Mg alloys subjected to loading along three different strain paths. Acta Mater. 55, 3899–3910.
Jiang, L., Jonas, J.J., Luo, A.A., Sachdev, A.K., Godet, S., 2007b. Influence of {1012} extension twinning on the flow behavior of AZ31 Mg alloy. Mater. Sci. Eng. A 445–446, 302–309.
Kabirian, F., Khan, A.S., Gnäupel-Herlod, T., 2015. Visco-plastic modeling of mechanical responses and texture evolution in extruded AZ31 magnesium alloy for various loading conditions. Int. J. Plast. 68, 1–20.
Kalidindi, S.R., 1998. Incorporation of deformation twinning in crystal plasticity models. J. Mech. Phys. Solids 46, 267–290.
Kalidindi, S.R., 2001. Modeling anisotropic strain hardening and deformation textures in low stacking fault energy fcc metals. Int. J. Plast. 17, 837–860.
Kalidindi, S.R., Bronkhorst, C.A., Anand, L., 1992. Crystallographic texture evolution in bulk deformation processing of FCC metals. J. Mech. Phys. Solids 40, 537–569.
Karaman, I., Sehitoglu, H., Beaudoin, A.J., Chumlyakov, Y.I., Maier, H.J., Tomé, C.N., 2000. Modeling the deformation behavior of Hadfield steel single and polycrystals due to twinning and slip. Acta Mater. 48, 2031–2047.
Kelley, E.W., Hosford, W.F., 1968. The deformation characteristics of textured magnesium. Trans. Metall. Soc. AIME 242, 654–661.
Keshavarz, Z., Barnett, M.R., 2006. EBSD analysis of deformation modes in Mg–3Al–1Zn. Scr. Mater. 55, 915–918.
Khan, A.S., Pandey, A., Gnäupel-Herold, T., Mishra, R.K., 2011. Mechanical response and texture evolution of AZ31 alloy at large strains for different strain rates and temperatures. Int. J. Plast. 27, 688–706.
Khan, A.S., Yu, S., 2012. Deformation induced anisotropic responses of Ti–6Al–4V alloy. Part I: Experiments. Int. J. Plast. 38, 1–13.
Khosravani, A., Fullwood, D.T., Adams, B.L., Rampton, T.M., Miles, M.P., Mishra, R.K., 2015. Nucleation and propagation of {1012}twins in AZ31 magnesium alloy. Acta Mater. 100, 202–214.
Knezevic, M., Levinson, A., Harris, R., Mishra, R.K., Doherty, R.D., Kalidindi, S.R., 2010. Deformation twinning in AZ31: influence on strain hardening and texture evolution. Acta Mater. 58, 6230–6242.
Knezevic, M., Zecevic, M., Beyerlein, I.J., Bingert, J.F., McCabe, R.J., 2015. Strain rate and temperature effects on the selection of primary and secondary slip and twinning systems in HCP Zr. Acta Mater. 88, 55–73.
Koike, J., Kobayashi, T., Mukai, T., Watanabe, H., Suzuki, M., Maruyama, K., Higashi, K., 2003. The activity of non-basal slip systems and dynamic recovery at room temperature in fine-grained AZ31B magnesium alloys. Acta Mater. 51, 2055–2065.
Kumar, M.A., Capolungo, L., McCabe, R.J., Tomé, C.N. Characterizing the role of adjoining twins at grain boundaries in hexagonal close packed materials.2019 Sci. Rep. 9:3846, 1-10..
Lebensohn, R.A., 1999. Modelling the role of local correlations in polycrystal plasticity using viscoplastic self-consistent schemes. Model. Simul. Mater. Sci. Eng. 7, 739–746.
Lou, X.Y., Li, M., Boger, R.K., Agnew, S.R., Wagoner, R.H., 2007. Hardening evolution of AZ31B Mg sheet. Int. J. Plast. 23, 44–86.

Ma, Q., El Kadiri, H., Oppedal, A.L., Baird, J.C., Li, B., Horstemeyer, M.F., Vogel, S.C., 2012. Twinning effects in a rod-textured AM30 Magnesium alloy. Int. J. Plast. 29, 60–76.
Martin, É., Capolungo, L., Jiang, L., Jonas, J.J., 2010. Variant selection during secondary twinning in Mg–3%Al. Acta Mater. 58, 3970–3983.
Mason, T.A., Bingert, J.F., Kaschner, G.C., Wright, S.I., Larsen, R.J., 2002. Advances in deformation twin characterization using electron backscattered diffraction data. Metall. Mater. Trans. A 33, 949–954.
Mayama, T., Noda, M., Chiba, R., Kuroda, M., 2011. Crystal plasticity analysis of texture development in magnesium alloy during extrusion. Int. J. Plast. 27, 1916–1935.
McCabe, R.J., Proust, G., Cerreta, E.K., Misra, A., 2009. Quantitative analysis of deformation twinning in zirconium. Int. J. Plast. 25, 454–472.
Mercier, S., Toth, L.S., Molinari, A., 1995. Modelling of texture development and deformation mechanisms in a Ti20V alloy using a self consistent polycrystal approach. Textures Microstruct. 25, 45–61.
Mokdad, F., Chen, D.L., Li, D.Y., 2017. Single and double twin nucleation, growth, and interaction in an extruded magnesium alloy. Mater. Des. 119, 376–396.
Molinari, A., Canova, G.R., Ahzi, S., 1987. A self consistent approach of the large deformation polycrystal viscoplasticity. Acta Metall. 35, 2983–2994.
Molinari, A., Toth, L.S., 1994. Tuning a self consistent viscoplastic model by finite element results-I. Modeling. Acta Metall. 42, 2453–2458.
Molinari, A., El Houdaigui, F., Toth, L.S., 2004. Validation of the tangent formulation for the solution of the non-linear Eshelby inclusion problem. Int. J. Plast. 20, 291–307.
Molodov, K.D., Al-Samman, T., Molodov, D.A., 2017. Profuse slip transmission across twin boundaries in magnesium. Acta Mater. 124, 397–409.
Morozumi, S., Kikuchi, M., Yoshinaga, H., 1976. Electron microscope observation in and around {1102}twins in Magnesium. Trans. JIM 17, 158–164.
Mu, S., Al-Samman, T., Mohles, V., Gottstein, G., 2011. Cluster type grain interaction model including twinning for texture prediction: application to magnesium alloys. Acta Mater. 59, 6938–6948.
Mu, S., Tang, F., Gottstein, G., 2014. A cluster-type grain interaction deformation texture model accounting for twinning-induced texture and strain-hardening evolution: application to Magnesium alloys. Acta Mater. 68, 310–324.
Nadella, R.K., Samajdar, I., Gottstein, G., 2003. Static recrystallisation and textural changes in warm rolled pure magnesium. Mg. Proc. ICMA 1052–1057.
Nave, M.D., Barnett, M.R., 2004. Microstructures and textures of pure magnesium deformed in plane-strain compression. Scr. Mater. 51, 881–885.
Niewczas, M., 2010. Lattice correspondence during twinning in hexagonal close-packed crystals. Acta Mater. 58, 5848–5857.
Obara, T., Yoshinga, H., Morozumi, S., 1973. {1122}1123 Slip system in magnesium. Acta Metall. 21 (7), 845–853.
Oppedal, A.L., El Kadiri, H., Tomé, C.N., Kaschner, G.C., Vogel, S.C., Baird, J.C., Horstemeyer, M.F., 2012. Effect of dislocation transmutation on modeling hardening mechanisms by twinning in magnesium. Int. J. Plast. 30–31, 41–61.
Ostapovets, A., Šedá, P., Jäger, A., Lejček, P., 2011. Characteristics of coincident site lattice grain boundaries developed during equal channel angular pressing of magnesium single crystals. Scr. Mater. 64, 470–473.
Ostapovets, A., Šedá, P., Jäger, A., Lejček, P., 2012. New misorientation scheme for a visco-plastic self-consistent model: equal channel angular pressing of magnesium single crystals. Int. J. Plast. 29, 1–12.
Paramatmuni, C., Kanjarla, A.K., 2018. A crystal plasticity FFT based study of deformation twinning, anisotropy and micromechanics in HCP materials: application to AZ31 alloy. Int. J. Plast. 113, 269–290.
Parisot, R., Forest, S., Pineau, A., Grillon, F., Demonet, X., Mataigne, J.M., 2004. Deformation and damage mechanisms of zinc coatings on hot-dip galvanized steel sheets: Part I. Deformation modes. Metall. Mater. Trans. A 35, 797–811.
Park, S.H., Hong, S.-G., Lee, C.S., 2010. Activation mode dependent {1012}twinning characteristics in a polycrystalline magnesium alloy. Scr. Mater. 62, 202–205.
Pei, Y., Godfrey, A., Jiang, J., Zhang, Y.B., Liu, W., Liu, Q., 2012. Extension twin variant selection during uniaxial compression of a magnesium alloy. Mater. Sci. Eng. A 550, 138–145.
Proust, G., Tomé, C.N., Jain, A., Agnew, S.R., 2009. Modeling the effect of twinning and detwinning during strain-path changes of magnesium alloy AZ31. Int. J. Plast. 25, 861–880.
Proust, G., Tomé, C.N., Kaschner, G.C., 2007. Modeling texture, twinning and hardening evolution during deformation of hexagonal materials. Acta Mater. 55, 2137–2148.
Raabe, D., 1998. Computational Materials Science-The Simulation of Materials, Microstructures and Properties. Wiley-VCH, pp. 267–300.
Robson, J.D., Stanford, N., Barnett, M.R., 2010. Effect of particles in promoting twin nucleation in a Mg–5wt.% Zn alloy. Scr. Mater. 63, 823–826.
Roters, F., Eisenlohr, P., Hantcherli, L., Tjahjanto, D.D., Bieler, T.R., Raabe, D., 2010. Overview of constitutive laws, kinematics, homogenization and multiscale methods in crystal plasticity finite-element modeling: theory, experiments, applications. Acta Mater. 58, 1152–1211.
Sahoo, S.K., Toth, L.S., Biswas, S., 2019. An analytical model to predict strain-hardening behaviour and twin volume fraction in a profoundly twinning magnesium alloy. Int. J. Plast. 119, 273–290.
Salem, A.A., Kalidindi, S.R., Doherty, R.D., 2003. Strain hardening of Titanium: role of deformation twinning. Acta Mater. 51, 4225–4237.
Srivastava, K., El-Awady, J.A., 2017. Deformation of magnesium during c-axis compression at low temperatures. Acta Mater. 133, 282–292.
Tadano, Y., Yoshihara, Y., Hagihara, S., 2016. A crystal plasticity modeling considering volume fraction of deformation twinning. Int. J. Plast. 84, 88–101.
Taylor, G.I., 1938. Plastic strain in metals. J. Inst. Met. 62, 307–324.
Tomé, C.N., Kaschner, G.C., 2005. Modeling texture, twinning and hardening evolution during deformation of hexagonal materials. Mater. Sci. Forum 495–497, 1001–1006.
Tomé, C.N., Lebensohn, R.A., Kocks, U.F., 1991. A model for texture development dominated by deformation twinning: application to zirconium alloys. Acta Metall. 39, 2667–2680.
Tomé, C.N., Maudlin, P.J., Lebensohn, R.A., Kaschner, G.C., 2001. Mechanical response of zirconium-I. Derivation of a polycrystal constitutive law and finite element analysis. Acta Mater. 49, 3085–3096.
Toth, L.S., Beausir, B., Gu, C.F., Estrin, Y., Scheerbaum, N., Davies, C.H.J., 2010. Effect of grain refinement by severe plastic deformation on the next-neighbor misorientation distribution. Acta Mater. 58, 6706–6716.
Toth, L.S., Haase, C., Allen, R., Lapovok, R., Molodov, D.A., Cherkaoui, M., El Kadiri, H., 2018. Modeling the effect of primary and secondary twinning on texture evolution during severe plastic deformation of a twinning-induced plasticity steel. Materials 11, 863.
Toth, L.S., Molinari, A., Raabe, D., 1997. Modeling of rolling texture development in a ferritic chromium steel. Metall. Mater. Trans. A 28, 2343–2351.
Ulacia, I., Dudamell, N.V., Gálvez, F., Yi, S., Pérez-Prado, M.T., Hurtado, I., 2010. Mechanical behavior and microstructural evolution of a Mg AZ31 sheet at dynamic strain rates. Acta Mater. 58, 2988–2998.
Van Houtte, P., 1978. Simulation of the rolling and shear texture of brass by the Taylor theory adapted for mechanical twinning. Acta Metall. 26, 591–604.
Wang, F., Agnew, S.R., 2016. Dislocation transmutation by tension twinning in magnesium alloy AZ31. Int. J. Plast. 81, 63–86.
Wang, H., Raeisinia, B., Wu, P.D., Agnew, S.R., Tomé, C.N., 2010. Evaluation of self-consistent polycrystal plasticity models for magnesium alloy AZ31B sheet. Int. J. Solids Struct. 47, 2905–2917.
Wang, B., Xin, R., Huang, G., Liu, Q., 2012. Effect of crystal orientation on the mechanical properties and strain hardening behavior of magnesium alloy AZ31 during uniaxial compression. Mater. Sci. Eng. A 534, 588–593.
Wright, S.I., Nowell, M.M., Field, D.P., 2011. A review of strain analysis using electron backscatter diffraction. Microsc. Microanal. 17, 316–329.
Xie, K.Y., Alam, Z., Caffee, A., Hemker, K.J., 2016. Pyramidal I slip in c-axis compressed Mg single crystals. Scr. Mater. 112, 75–78.
Xin, R., Ding, C., Guo, C., Liu, Q., 2016. Crystallographic analysis on the activation of multiple twins in rolled AZ31 Mg alloy sheets during uniaxial and plane strain compression. Mater. Sci. Eng. A 652, 42–50.
Yi, S., Brokmeier, H.-G., Letzig, D., 2010. Microstructural evolution during the annealing of an extruded AZ31 magnesium alloy. J. Alloy. Comp. 506, 364–371.
Yoo, M.H., 1981. Slip, twinning, and fracture in hexagonal close-packed metals. Metall. Trans. A 12, 409–418.
Zhang, J., Joshi, S.P., 2012. Phenomenological crystal plasticity modeling and detailed micromechanical investigations of pure magnesium. J. Mech. Phys. Solids 60, 945–972.

Zhang, J., Xi, G., Wan, X., Fang, C., 2017. The dislocation-twin interaction and evolution of twin boundary in AZ31 Mg alloy. Acta Mater. 133, 208–216.
Zhu, K.Y., Bacroix, B., Chauveau, T., Chaubet, D., Castelnau, O., 2009. Texture evolution and associated nucleation and growth mechanisms during annealing of a Zr Alloy. Metall. Mater. Trans. A 40, 2423–2434.
Zhou, Y., Neale, K.W., Toth, L.S., 1993. A modified model for simulating latent hardening during the plastic deformation of rate-dependent FCC polycrystals. Int. J. Plast. 9, 961–978.
Zilahi, Gy, 2018. Three-dimensional Line Profile Analysis. PhD Thesis. Eotvos University, Budapest, Hungary.